Memoirs of the Faculty of Science, Kyoto University, Series of Physics, Astrophysics, Geophysics and Chemistry, Vol. XXXIX, No. 2, Article 3, 1995

Measurements of the Double-Spin Asymmetry A_{LL} and the Invariant Double-Differential Cross Section for Inclusive Multi-γ Pair Production with 200-GeV/c Polarized Proton Beam and Polarized Proton Target

By

Seiji MAKINO*

Department of Physics, Faculty of Science, Kyoto University, Kyoto 606-01, Japan

(Received December 12, 1994)

Abstract

The invariant double-differential cross section, $E_1E_2d^6\sigma/dp_1^3dp_2^3$, and the double-spin asymmetry, A_{LL}, for inclusive multi-γ pair production were measured with two sets of lead-glass calorimeters at $\pm 90^\circ$ in the center of mass frame of a 200-GeV/c longitudinally-polarized proton beam and a longitudinally-polarized proton target in the Fermilab Spin Physics Facility. We define the "multi-γ" as a set of one or more γ-rays detected in one of the electromagnetic calorimeters. A multi-γ pair event is defined as an event in which multi-γ's are detected with calorimeters on both sides of the beam axis. The invariant double-differential cross section for inclusive $\pi^0\pi^0$ production was also measured. The $\pi^0\pi^0$ events have been obtained as a subset of multi-γ pair events. The measured cross sections are consistent with the results from the LUND Monte-Carlo simulations. The obtained A_{LL} have been found to be consistent with zero. The behavior of A_{LL} has been compared with several theoretical predictions of the gluon polarization, $\Delta G/G$, using the LUND Monte-Carlo simulation package and the Carlitz-Kaur model of the spin dependent distribution functions of valence quarks. The results put a restriction on $\Delta G/G$ in the x region of 0.05 to 0.35.

1. Introduction

A large amount of data for the test of the quantum chromodynamics (QCD) has been accumulated through many experiments with high energy hadron beams at CERN and Fermi National Accelerator Laboratory (FNAL). In particular, hard collisions have been studied in productions of jets, prompt photons, lepton pairs and heavy quarks. Information on the parton structure of proton was obtained from these data, often beyond leading order. In addition to the measurements of cross sections, it is important to measure the spin related parameters using polarized beams and targets in order to study the spin structure of the proton.

Available facilities for studying the spin structure of hadron were very few before 1990. Regarding inclusive measurements of hadronic interactions, polarized proton

* Present address: Wakayama Medical College, 651 Hironishi, Wakayama 649-63, Japan.

beams of 6 GeV/c and 11.8 GeV/c from ZGS[1] and those of momenta up to 22 GeV/c from AGS[2] provided useful experimental data on spin parameters. Polarized proton targets were used with unpolarized proton beam of 24 GeV/c at CERN[3] and with π^- beam of 40 GeV/c at Institute for High Energy Physics (IHEP), Protovino in Russia[4]. Some of the experimental results using these facilities showed significant spin effects. The presence of these large spin effects is considered to be originated from complicated processes which include the collisions different from partonic interactions. In order to investigate the spin effects in partonic interactions where the perturbative QCD picture is applicable, it is indispensable to go to higher energy region.

The polarized quark density, Δq, in proton was studied with a polarized electron beam and a polarized proton target in the x region of 0.1 to 0.7 (E80 and E130 at SLAC)[5] and with a polarized muon beam and a polarized proton target in the smaller x region of 0.01 to 0.7 (European Muon Collaboration (EMC) at CERN)[6]. The Spin Muon Collaboration (SMC) at CERN[7] and E142/E143 at SLAC[8] have been trying to measure asymmetries in still smaller x region. By comparing the experimental results with the Bjorken sum rule[9] and the Ellis-Jaffe sum rule[10], it is shown that the contribution of quark spins to the proton spin is not large.

The polarized gluon density, ΔG, may also be the origin of the proton spin. The contribution of the gluon spin to the proton spin must be also investigated experimentally. One of the promising ways to solve the problem is to measure spin parameters of proton-proton reactions in which the gluonic terms are dominant[11].

The E704 experiment was carried out at the Fermilab Spin Physics Facility. Several spin parameters measured with a 200-GeV/c polarized proton beam in this experiment are very useful for the investigation of the spin structure of proton. Here, we focus on the measurement of the double-spin asymmetry, A_{LL}, which has become possible using the high-energy polarized proton beam and the polarized proton target for the first time. The double-spin asymmetry, A_{LL}, indicates the asymmetry of cross sections with the same and opposite helicity combinations of beam and target protons in the center of mass frame. The importance of the A_{LL} measurements in inclusive reactions of hard hadronic collisions is in the fact that the parameter is related directly to the gluon polarization.

In a previous paper[12], we reported the double-spin asymmetry, A_{LL}, for inclusive π^0 production using longitudinally-polarized proton and anti-proton beams with a longitudinally-polarized proton target. These data agree better with theoretical predictions which assume small or zero gluon polarization than with those which assume large gluon polarization. The data, however, could not distinguish among models of the gluon polarization clearly because the sensitivity of the parameter to the gluon polarization is not significantly large. In this energy region, most of hard collisions are considered to produce two-jet type fragmentation. In the case of inclusive measurement of one jet, the information of parton distribution is smeared out due to the other undetected jet. On the other hand, in the measurement of two jets, there is no serious problem of smearing and measured spin parameters become sensitive to partonic interactions, especially to gluonic terms as discussed theoretically in Ref. 13.

We report on the measurements of the invariant double-differential cross section,

$E_1E_2d^6\sigma/d\boldsymbol{p}_1{}^3d\boldsymbol{p}_2{}^3$, and the double-spin asymmetry, A_{LL}, for inclusive multi-γ pair production with the longitudinally-polarized proton beam and the longitudinally-polarized proton target[14]. Two sets of lead-glass Čerenkov counter arrays were used for the detection of γ-rays. Multi-wire proportional chambers were used for the detection of charged particles. These detectors were placed in the directions of $\pm 90°$ in the center of mass frame of beam and target protons. We define "multi-γ" as a set of one or more γ-rays detected in one of the electromagnetic calorimeters which is described in Section 2.2.2.1. Most of the γ-rays are decay products of π^0 and η mesons as shown in Section 4.5. The multi-γ pair event is defined as the event in which multi-γ's are detected with the calorimeters on both sides of the beam axis. The pseudo-mass, M', and the pair transverse momentum, p_T', are defined as

$$M' = |p_{T_1}| + |p_{T_2}|, \tag{1}$$

$$p_T' = |p_{T_1}| - |p_{T_2}|, \tag{2}$$

where p_{T_1} and p_{T_2} are the transverse momenta of each multi-γ. We measured the double-spin asymmetry and the cross section as a function of M' in the region of 2.0 GeV/c to 4.0 GeV/c and $|p_T'| < 1.0$ GeV/c.

In this measurement, each multi-γ comes mainly from one jet in a two-jet production. Consequently, the measurement of A_{LL} for the multi-γ pair production is sensitive to the polarization of quarks and gluons.

Our results of A_{LL} for inclusive multi-γ pair production have been compared with theoretical estimations using various $\Delta G/G$ models[15,16,17,18,19] with the help of the LUND Monte-Carlo simulation package (PYTHIA version 5.4 and JETSET version 7.3). We discuss the amplitude of ΔG based on this comparison.

We report also on the experimental results of the invariant double-differential cross section for inclusive $\pi^0\pi^0$ production. It is worthwhile to check the LUND Monte-Carlo simulation used in the present analyses with our experimental data on inclusive $\pi^0\pi^0$ production. The $\pi^0\pi^0$ events have been obtained as a subset of multi-γ pair events, where two π^0 mesons have been reconstructed. We measured the cross section of this reaction as a function of M' which is defined in the same way as in the case of multi-γ pair events.

The characteristics of the beam line and the detectors is shown in Chapter 2. The explanation of the triggers and the data acquisition system for the data taking is written in Chapter 3. The data analyses including the method of finding π^0 mesons and multi-γ pairs are described in Chapter 4. The experimental results are presented in Chapter 5 where discussions are given based on the model comparison.

2. Experimental Setup

In this chapter, we explain the Fermilab Spin Physics Facility including the detectors used in the present work.

2.1 Polarized Proton Beam and Beam Tagging System

The Fermilab Spin Physics Facility provides a 200-GeV/c polarized proton

beam[20]. To measure the momentum and polarization of each proton, this beam line has a tagging station. In order to rotate the spin of proton for the measurement, the magnet system, "snake magnets", is used.

2.1.1 Beam Line

In TEVATRON at FNAL, protons are accelerated up to 800 GeV/c. One acceleration cycle is 60 seconds. In each cycle, the proton beam is extracted in 20 seconds. The proton beam is transported to a beryllium wire target and produces Λ hyperons. The beryllium wire target has a horizontal width of 1.5 mm, a vertical hight of 5 mm and is 30.0 cm long. In the decay region of 20 m, approximately half of Λ hyperons decay into protons and π^- mesons in the energy region which we are interested in (Fig. 1). The polarization of outgoing protons is 64% with the spin direction along the proton momentum in the Λ rest frame because of parity violation in the weak interaction.

In the laboratory frame, the trajectories of the protons from the Λ decays can be traced back to the vertical plane at the position of the production target as schematically shown in Fig. 2. Here, the protons are considered to come from a "virtual source" displaced from the actual Λ source. For the fixed decay length of Λ hyperons, the protons with the same transverse spin component come from the same point on the "virtual source", regardless of the direction of Λ hyperons. The spin component of each proton transverse to the beam axis is, therefore, correlated to its projected position at the "virtual source".

Those protons are transported over the neutral particle dump to the tagging station. The center value of the momentum of this polarized proton beam is tuned to 200 GeV/c and the momentum bite is 9.6%. This beam line provides the highest energy polarized proton beam in the world.

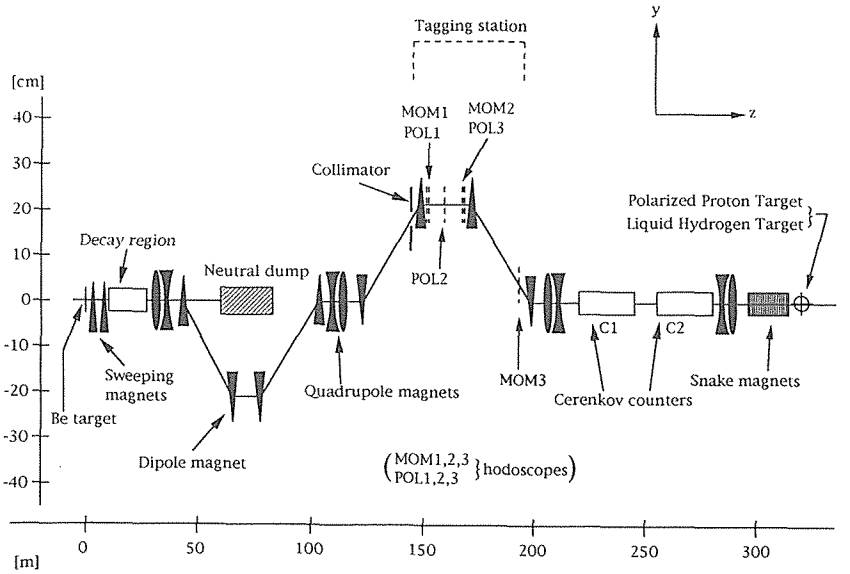

Fig. 1. Schematic side view of the polarized proton beam line.

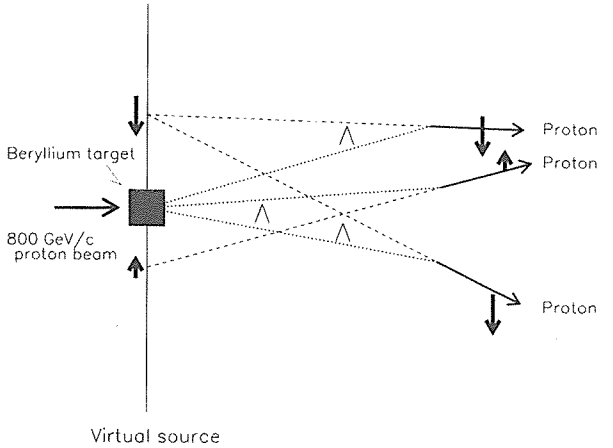

Fig. 2. Mechanism to obtain the polarized beam from the decay of Λ hyperons. The Λ hyperons (dotted lines) which are produced with a 800-GeV/c proton beam on a beryllium target decay into protons (solid lines) and π^- mesons (not shown). The polarization of the proton is correlated with the position in the plane of the "virtual source" which is the traced-back image (dashed lines) from the proton trajectories.

2.1.2 Beam Tagging System

The polarized beam line has the tagging station at 150 m from the beryllium target to make a tag of momentum and polarization for each beam proton (Fig. 1). At the tagging station, the momentum and polarization of a proton are measured using plastic scintillator hodoscopes (POL1, POL2 and POL3 for polarization measurement and MOM1, MOM2 and MOM3 for momentum measurement). The tagging station is placed at the intermediate focal point of the polarized beam line. The image of the "virtual source" can be seen at the tagging station. The horizontal size of the production target of Λ hyperons is made smaller than the vertical size and the proton polarization is correlated to the horizontal position on the plane of the "virtual source". The polarization is tagged as the horizontal position of beam proton using POL1 and POL3. The POL2 detector was used as the redundancy check. The distribution of tagged polarization is shown in Fig. 3 (a). The momentum of beam proton is also measured as the bending angle in the vertical plane using MOM1, MOM2 and MOM3. The distribution of tagged momentum is shown in Fig. 3 (b). After the tagging station, the spin direction is horizontal (S type). For convenience, we divide the beam into three categories using the tagging information of polarization. The positive polarization is defined that the spin direction of protons is $+x$ and the polarization value is between $+35\%$ and $+65\%$. The average polarization in this region is $+45\%$. The negative polarization is defined that the spin direction of protons is $-x$ and the polarization value is between -35% and -65%. The protons in this region have an average polarization of -45%. The zero polarization is defined that the polarization value is between -35% and $+35\%$ with an average of 0%.

Two threshold-type Čerenkov counters filled with helium gas of 0.3 atm. are placed at 250 m from the beryllium target. The pressure is set so as to produce signals when

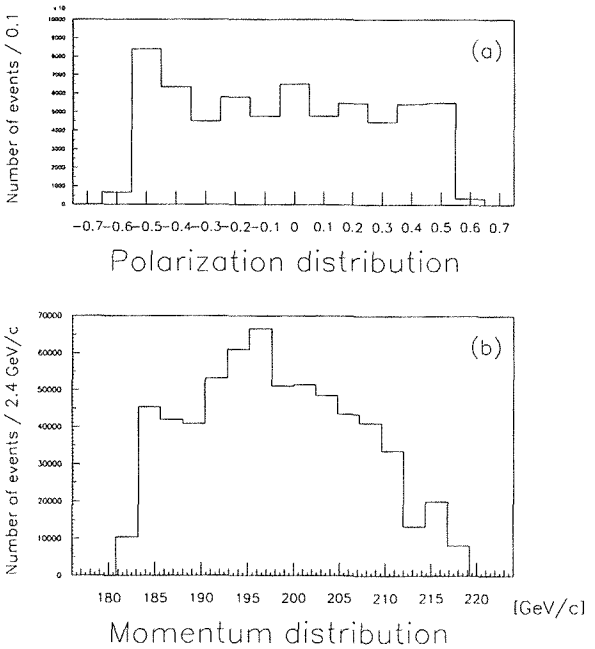

Fig. 3. (a) The distribution of tagged polarization of protons (10% bins). (b) The distribution of tagged momentum of polarized protons (2.4 GeV/c bins).

beam particles are π^+ mesons, and not to produce signals when beam particles are protons. Using the signals from them, the contamination of π^+ mesons is eliminated.

2.1.3 Snake Magnets and Beam-Defining System

The spin rotation magnets, "snake magnets", are placed between the Čerenkov counters and the experimental target at 300 m from the beryllium target. The magnet system consists of twelve dipole magnets. Each magnet has a 10.2 cm gap, a 22.9 cm aperture and is 99.1 cm long. It has 13.8-kG magnetic field. The pole faces of the magnets are tilted $\pm 45°$ with respect to the vertical axis. Each magnet gives a 45° rotation of spin about the direction of the magnetic field. When all magnets are used, the direction of polarization is changed from horizontal (S type) to longitudinal (L type). The combination of the magnet excitations is chosen to cancel the bend and displacement of the trajectory while beam particles traverse the snake magnets.

By reversing the polarities of the snake magnets, the spin direction of particles at the target changes to the opposite sign. During the actual data taking period, we reversed the polarities every 12 minutes in order to cancel possible geometric bias and to minimize the effect of time-dependent drifts of the performance of the apparatus.

Two sets of scintillation counter hodoscopes, SH1 and SH2, called "snake hodoscopes", were placed at 23 m and at 3 m upstream the experimental target, respectively (Fig. 4). We used them for tracking the beam. The two multi-wire proportional chambers (MWPC's), BK1 and BK2, were also used for tracking beam particles. The BK1 and BK2 were placed at 23 m and at 2.2 m upstream the experimental target, respectively. Both BK1 and BK2 have x and y planes. Gas of

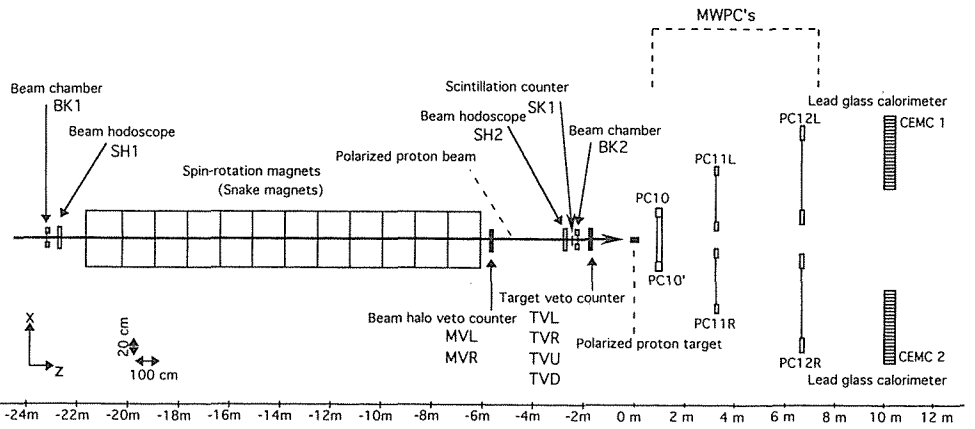

Fig. 4. Vertical view of the experimental setup.

83% argon, 15% iso-butane and 2% freon-13B1 with a methylal bubbler were used for BK1 and BK2.

The scintillation counter, SK1, was placed just in front of BK2. The shape of SK1 was square and the size was 5×5 cm^2. This counter was also used for defining the beam.

A counter to veto beam halos, MV, consisted of two scintillators (MVL and MVR). It had a hole of 6 cm in diameter around the beam center. It was placed just downstream the snake magnets. A target veto counter, TV, consisted of four scintillators (TVL, TVR, TVU and TVD). It had a hole of 3 cm in diameter around beam center and was placed just downstream BK2. It was used to define the beam size.

2.2 Experimental Targets and Detectors

The experimental setup for the measurement for inclusive $\pi^0\pi^0$ production and inclusive multi-γ pair production is shown in Fig. 4. Two sets of the lead glass counter arrays, CEMC1 and CEMC2, were placed on right and left sides of the beam axis for detecting γ-rays. The MWPC's, PC10, PC10', PC11L, PC11R, PC12L and PC12R, were placed in front of the lead glass detectors for tracking charged particles. A polarized proton target (PPT) was used for A_{LL} measurements with the longitudinally-polarized beam.

2.2.1 Polarized Proton Target

The size of PPT was 3 cm in diameter and was 20 cm long. It contained chromium-V doped pentanol ($C_5H_{12}O$). Free protons in the target material were polarized at the temperature of 400 mK with the microwaves of 70 GHz in the magnetic field of 25 kG of the polarizing solenoid at the position of the "polarizing mode" as shown in Fig. 5. After the maximum polarization was obtained, the solenoid was moved to upstream and the target was kept polarized without microwaves as a "frozen spin target". The frozen spin mode was kept at the temperature below 80 mK and in the magnetic field of 7 kG. In this condition, the proton spin relaxation time was longer than 50 days. The polarization was monitored using a nuclear magnetic

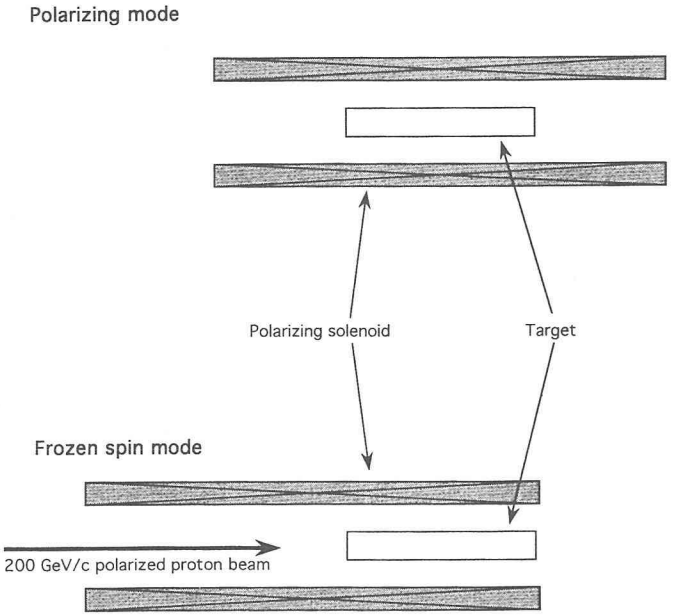

Fig. 5. Schematic drawing of the polarizing solenoid at the polarizing mode and at the frozen spin mode.

resonance (NMR) method in each run. The sign of the polarization direction was reversed every few days in order to reduce possible systematic errors. During the beam time, the average polarization observed was -0.808 ± 0.026 for the negative polarization and $+0.780\pm0.025$ for the positive one. The measured polarization value in each run was used in the data analyses.

The "target constant" of the PPT which is defined as $A/(\rho l N_A)$, where A, ρ, l and N_A are the atomic number, target density, target length and Avogadro's number, respectively, was $(1040\pm38)\times10^9$ pb. The ratio of the number of all nucleons to the number of free protons in the target material is defined as the dilution factor, D, which is 88/12.

2.2.2 Detectors in the Experimental Setup

2.2.2.1 Lead Glass Calorimeters

Outgoing γ-rays were detected using Central Electromagnetic Calorimeters, CEMC1 and CEMC2, which were placed on the left and the right sides of the beam axis, respectively (Fig. 4). The front surfaces of the CEMC's were placed at 10 m from the target center. The distance between the beam center and the center of each lead-glass array was 0.97 m. Each CEMC covered the polar angle of $5.5^\circ\pm2.2^\circ$ and the azimuthal angle of $\pm25^\circ$ in the laboratory frame. The center of each CEMC corresponded to 90° in the center of mass system of the beam and the target.

Each calorimeter consisted of lead-glass Čerenkov counters in an array of 21 columns by 24 rows. For monitoring the gain drift of the counters in each CEMC, two americium-NaI light sources and a light emission diode (LED) were used. The light from the LED was distributed via optical fibers to 21×24 counters in the array and two additional counters which were equipped with the americium-NaI. We found the gain

Table 1. The composition of lead glass (TF1-000) and its parameters

SiO_2	31.6%	Size [cm^3]	$3.81\times3.81\times45.0$
As_2O_3	0.2%	Density [g/cm^3]	3.86
PbO	65.4%	Index	1.67
K_2O	2.8%	X_0 [cm]	2.50
		E_{crit} [MeV]	15.80

stability was within a few percent during the runs.

Each array of the lead glass counters was placed in a movable dark box. The cold nitrogen gas was flowing in the box for stabilization of temperature. The average temperature of CEMC1 and CEMC2 was 26° and the stability was ±2° during the beam time.

The lead glass counters were TF1-000 made at IHEP. The characteristics of the lead glass material are shown in Table 1. The radiation length of the material is 2.50 cm. The size of the counter is $3.81\times3.81\times45.0\,cm^3$. Each lead glass was wrapped with sheets of aluminized mylar of 20 μm in thickness. The Čerenkov lights from the lead glass blocks were detected using photomultiplier tubes, PHEU-84-3 (Russian), with twelve-stage Venetian-blind dynodes. The photocathode was S-200 of trialkali (Sb-K-Na-Cs) with the maximum sensitivity at 420 nm. Booster voltages were distributed to the last 4 dynodes of each photomultiplier tube in order to stabilize the potential levels of those dynodes.

The energy calibration of the lead glass counters was carried out using a 31-GeV positron beam produced with the 800-GeV/c proton beam on an aluminum target of 0.2 radiation length. The coefficients between the energy deposit and the pulse height (ADC count) were obtained using the calibration data. The energy of a positron, E, is obtained as

$$E=\sum_i E_i=\sum_i C_i\cdot A_i \tag{3}$$

where E_i is the energy deposit in each counter, A_i is the ADC count after the pedestal was subtracted and C_i is the calibration constant. Although the responses of the counters to LED lights were stable within a few percent, we made the gain calibration run by run using the LED data. The distribution of reconstructed energy obtained by 31-GeV positron beam is shown in Fig. 6. The energy resolution was about 3% (r.m.s.). This result together with the calibration at IHEP† was parametrized in an empirical formula as

$$\frac{\sigma(E)}{E}=1.0+\frac{12.0}{\sqrt{E}}\%. \tag{4}$$

We found that the position resolution was 1.5 mm (r.m.s.).

The maximum p_T coverage to reconstruct π^0 mesons in each CEMC is estimated as follows in the ideal case. Assume that π^0 decays at the target center into two γ-rays whose four momenta are defined as $(E_1, \boldsymbol{p}_1)$ and $(E_2, \boldsymbol{p}_2)$ in the laboratory frame.

† The obtained values of the energy resolution were 3% (r.m.s.) at the beam energy of 26.6 GeV and 2.5% at 40 GeV.

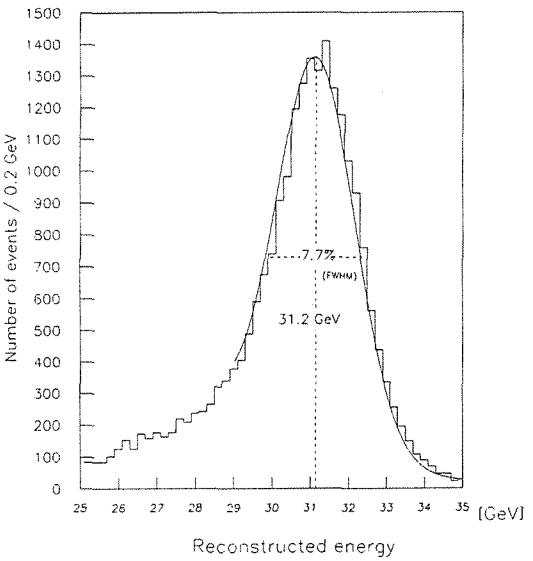

Fig. 6. The reconstructed energy distribution with 31 GeV positron beam.

Here, the distance between the hit positions of these γ-rays on the front surface of the lead glass array is given as d. The angle between $\boldsymbol{p}_1$ and $\boldsymbol{p}_2$ is given as θ. Then the invariant mass squared of two γ-rays is calculated as

$$m_{\gamma\gamma}{}^2 = m_{\pi^0}{}^2 = 2(E_1E_2 - \boldsymbol{p}_1 \cdot \boldsymbol{p}_2) \tag{5}$$

where

$$E_1 = |\boldsymbol{p}_1| \text{ and } E_2 = |\boldsymbol{p}_2|. \tag{6}$$

Using

$$\boldsymbol{p}_1 \cdot \boldsymbol{p}_2 = |\boldsymbol{p}_1||\boldsymbol{p}_2| \cos\theta = E_1E_2 \cos\theta, \tag{7}$$

the π^0 mass squared is written as

$$m_{\pi^0}{}^2 = 2E_1E_2(1-\cos\theta) = 4E_1E_2 \sin^2\frac{\theta}{2} \tag{8}$$

Using the distance between the target center and the lead glass array and the distance between two hit positions, d,

$$\sin\frac{\theta}{2} \approx \frac{d}{20}. \tag{9}$$

Consequently, we obtain

$$m_{\pi^0} \approx \frac{d}{10}\sqrt{E_1E_2}. \tag{10}$$

It is safe to assume that two γ-rays from a π^0 meson are reconstructed when d is larger than the counter size, namely, $d \gtrsim 0.0381$ [m]. When $E_1 = E_2$, and θ and d are minimum, the maximum detectable energies of each γ-ray and π^0 meson are calculated as

$$E_1 = E_2 \approx 35 \text{ [GeV]} \text{ and } E_{\pi^0} \approx 70 \text{ [GeV]}. \tag{11}$$

The maximum p_T of π^0 mesons which can, therefore, be reconstructed is approximately 7 GeV/c.

The x_F coverage of each CEMC is calculated from the acceptance of polar angle in the horizontal plane. Applying the fiducial cut written in Section 4.2.2, the coverage of polar angle was 97.0 ± 38.1 mrad and the corresponding x_F coverage was

$$-0.0350p_T<x_F<0.0536p_T. \tag{12}$$

2.2.2.2. Multi-wire Proportional Chambers

We used six sets of MWPC's, PC10 (x and y planes), PC10′ (x and y planes), PC11L (x, y and v planes), PC11R (x, y and v planes), PC12L (x, y, u and v planes) and PC12R (x, y, u and v planes) as shown in Fig. 4. The angles of wire directions from the y-axis are 0.0°, 90.0°, 28.1° and −28.1° for x, y, u and v planes, respectively. Argon gas was used with 0.3% of freon with a cooled methylal bubbler for PC11L and PC11R. Gas of argon-CO_2 mixture with freon-13B1 was used for PC10, PC10′, PC12L and PC12R. A typical detection efficiency of each plane of MWPC's was about 85%. The characteristics of MWPC's are summarized in Table 2.

Table 2. The parameters of MWPC's downstream the target (from upstream)

MWPC	Coordinate	Wire spacing	Sensitive area [mm]	Number of wires	Distance from the target [m]
PC10	x	2.00 [mm]	514.0	257	1.0
	y	2.00 [mm]	514.0	257	
PC10′	x	2.00 [mm]	514.0	257	1.0
	y	2.00 [mm]	514.0	257	
PC11L	x	1/13 [inch]	500.0	256	3.4
	y	1/13 [inch]	500.0	256	
	v	1/13 [inch]	627.0	320	
PC11R	x	1/13 [inch]	500.0	256	3.4
	y	1/13 [inch]	500.0	256	
	v	1/13 [inch]	627.0	320	
PC12L	y	2.00 [mm]	1026.0	512	6.6
	u	2.00 [mm]	1026.0	512	
	v	2.00 [mm]	1026.0	512	
	x	2.00 [mm]	770.0	384	
PC12R	y	2.00 [mm]	1026.0	512	6.6
	u	2.00 [mm]	1026.0	512	
	v	2.00 [mm]	1026.0	512	
	x	2.00 [mm]	770.0	384	

3. Triggers and Data Acquisition

In this chapter, we describe the scheme to trigger the high-mass pair events together with the data acquisition and the on-line monitoring. The scheme of the

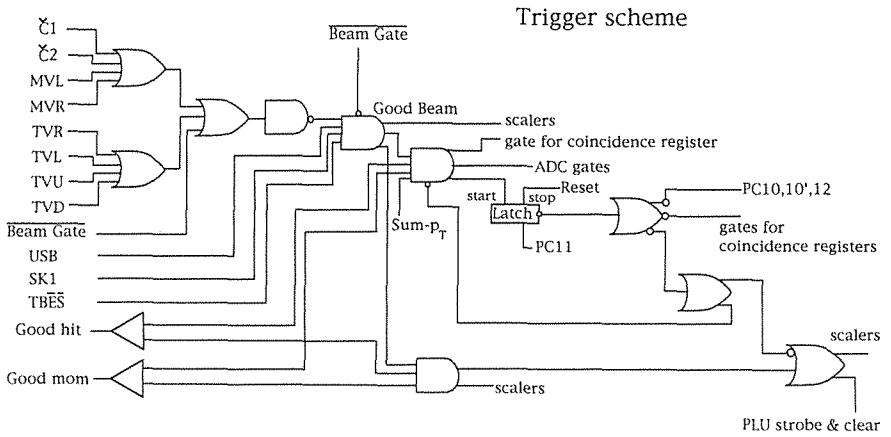

Fig. 7. Scheme of the event trigger.

"event trigger" as shown in Fig. 7 and Fig. 8 for taking interaction data is explained below.

3.1 Triggers for the Beam Particles

The "beam gate" signal indicated that the beam was on. The TBĒS signal was produced when a beam particle was separated from preceding particles by at least 60 nsec. The USB (Usable Snake Beam) signal showed that (a) there was one hit on each plane of SH1 and SH2, (b) it was not vetoed by the target veto counters (TVL, TVR, TVU, and TVD) and (c) Č1 and Č2 did not veto the particle. The SK1 signal indicated that the particle hit the scintillation counter, SK1. The Č1, Č2, the counter to veto beam halos (MVL and MVR) and the target veto counter (TVL, TVR, TVU, and TVD) formed veto signal for the beam trigger. The "beam gate", TBĒS, USB and SK1 with above veto signal produced the "good beam" signal.

The "good hit" signal and the "good mom" signal were produced at the tagging station and were sent to the data taking system using high speed cables (the speed of signals is 0.93 of the light velocity). The "good hit" signal indicated that there was

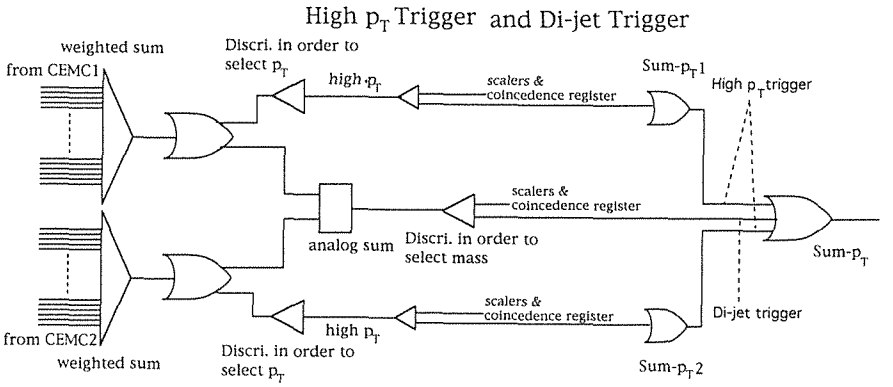

Fig. 8. Scheme of the "high p_T trigger" and the "di-jet trigger".

only one hit on each hodoscope of MOM1, MOM2, MOM3, POL1 and POL3. The "good mom" signal indicated that the calculation of the momentum of a beam particle was made successfully using a system with MLU's (memory lookup units) and PLU's (programmable logic units).

The "good beam", "good hit" and "good mom" signals produced "event trigger" with "high p_T trigger" and/or "di-jet trigger", which are described in Section 3.2.

3.2 High p_T Trigger and Di-jet Trigger

A signal which was proportional to the transverse momentum, p_T, of an electromagnetic shower was produced by the signals from the lead glass counters for each CEMC (Fig. 8).

Signals from the counters in same column were summed up with equal weight. The weighted sum signal which was approximately proportional to p_T was produced by the signals from the columns.

The signals of p_T above 1.6 GeV/c were discriminated from low p_T signals. The discriminated signals, "sum-p_T1" (from CEMC1) and "sum-p_T2" (from CEMC2), produced the "sum-p_T" signal. This was called as the "high p_T trigger" signal.

In addition, the "di-jet trigger" signal was composed to require simultaneous hits of γ-rays in both CEMC's (Fig. 8). The analog sum of p_T signals of both CEMC's was approximately proportional to the mass of high-mass pair. The signals of p_T sum

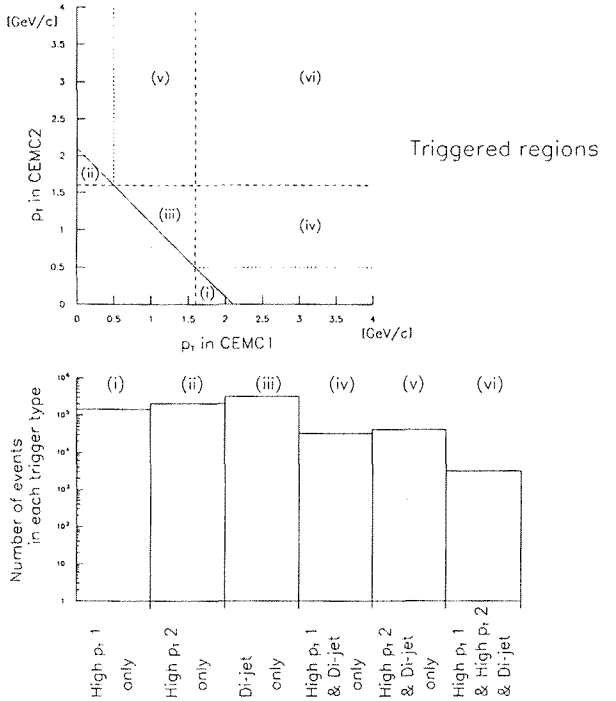

Fig. 9. The relation among the "high p_T trigger" for CEMC1, the "high p_T trigger" for CEMC2 and the "di-jet trigger". The trigger rates for each region are shown in the histogram exclusively.

above 2.1 GeV/c were discriminated from low p_T sum signals. The triggered regions in the plane of p_T in CEMC1 and p_T in CEMC2 are displayed in Fig. 9. The data of unbiased high-mass events were taken efficiently using the "di-jet trigger".

3.3 Data Taking and On-line Monitoring

A PDP-11 based data acquisition (DAQ) system was used to collect the data. According to each trigger type, required CAMAC modules were read out by the DAQ system. The data were sent to magnetic tapes (6250 bpi) from PDP-11.

The data taking was carried out in 1990. The typical beam intensity was about several times 10^5/sec during the measurement. The typical event rate was 22/sec. The scaler data were recorded together with the data of the lead-glass counters and the MWPC's. The pedestals of ADC and the data to monitor the lead-glass counters with the LED lights were taken in each spill before the beam was on. After the beam was off, the data of the lead glass counters with the lights from the americium-NaI sources were recorded. The data of the target polarization and the temperatures inside and outside the CEMC's were collected in each spill.

The detectors were monitored by an on-line system with the VAXstation 3200 which received sampled data from the DAQ system. The invariant mass of two γ-rays, hit positions and multiplicities of MWPC's were shown as histograms in order to confirm the condition of the detectors run by run, together with the calibration data using the LED and the americium-NaI sources.

4. Data Analysis

In this chapter, the method of the data analysis to obtain $\pi^0\pi^0$ events and multi-γ pair events is explained. First, events to be analyzed have been selected from all the data using the information of the beam counters (target cut). Then, the γ-rays have been reconstructed from the data of electromagnetic showers in CEMC's with the help of the shower table. Tracks of charged particles have been reconstructed from the data of MWPC's and a vertex in each event has been deduced.

4.1 Target Cut

Useful beam particles were selected using the signals from the tagging station as described in the previous chapter. Furthermore, we have applied the target cut in the analysis to eliminate beam halo events and events from the materials around the target. The x and y positions of each beam particle at the target have been derived from the data of SH1 and SH2. We have required ; $\sqrt{x^2+y^2} \leq 1.29$ [cm] to pick up the events from the target (target cut). The event distribution in x-y plane at the target is shown in Fig. 10. The circle indicates the boundary of the target cut. About 17% of events has been thrown away with this cut.

4.2 Shower Reconstruction

4.2.1 Shower Table

The electromagnetic shower table of the lead glass counters was made using the data obtained with 31-GeV positron beams. We measured the energy deposit of the

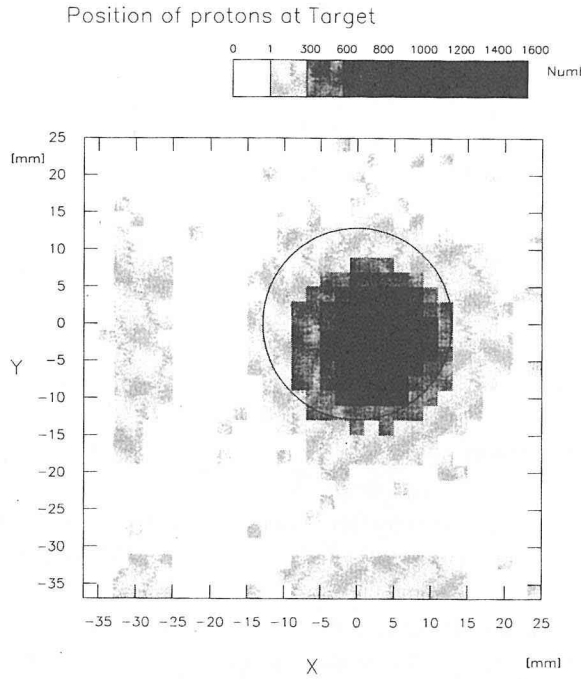

Fig. 10. The hit position of beam particles on the target reconstructed from the data of SH1 and SH2. The circle indicates the boundary of the target cut.

shower in the block of CEMC's in which the beam was put and also those in the surrounding eight blocks. The hit positions of the positrons on the front surface of the lead glass were determined with MWPC's.

The front surfaces of the lead glass blocks were divided into 25×25 small domains called "sub-cell" whose sizes were $0.152\times0.152\ \mathrm{cm}^2$. Each sub-cell is defined as (i, j) in the manner shown in Fig. 11, where i and j are the integers between 1 and 38. The

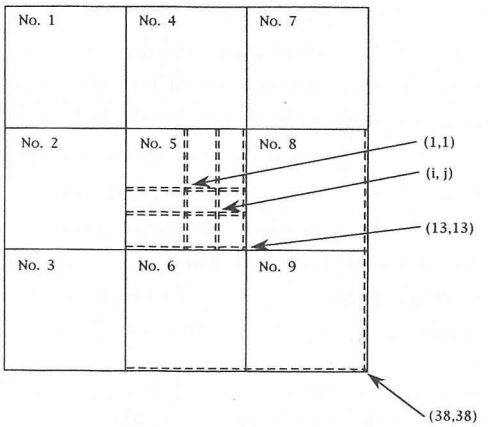

Fig. 11. The coordinate of the "sub-cell" in the lead glass counters.

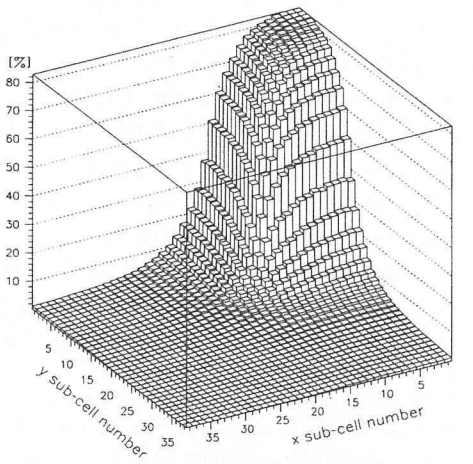

Fig. 12. The lego plot of the shower table.

central sub-cell is (1, 1).

The shower table was obtained for incident positrons on each sub-cell. Energy leakage of the shower from the 3×3 blocks was ignored in the shower reconstruction because the energy deposit outside the 3×3 blocks is smaller than a few percents of total energy of the shower. In the case when the positron hits the sub-cell (i, j) in the block No. 5 of Fig. 11, the numerical value on (i, j) in the shower table is given by the energy deposit in the block No. 5, and that on $(i+25, j+25)$ by the deposit in the block No. 1. Other numerical values on the shower table are also given in the same manner.

The shower table is made as a 38×38 array. The table is shown in Fig. 12 as a lego plot. When a positron hits the center $(i=j=1)$ of a counter, 80% of the energy is deposited in the counter in which the beam is put, and 24% when it hits at the edge $(i=j=13)$ of the counter.

4.2.2 Reconstruction Method

The data of counters containing energy deposit of more than 75 MeV have been used in the reconstruction of γ-rays (counter energy cut). The set of adjacent counters which have such an energy deposit is regarded as a cluster. When a cluster contained more than 500 MeV, it has been considered as a γ-ray candidate (cluster energy cut).

For a cluster spread not wider than 3×3 counters, the reconstruction of one γ-ray is carried out. The center of gravity of the energy deposit, (x, y), is derived. The position, (x, y), has the tendency to shift toward the center of the counter. The correction is made using the shower table information. The corrected position is regarded as the entrance position of the γ-ray. The total energy deposit is regarded as the energy of the γ-ray. Using the shower table with the corrected position, $\tilde{\chi}^2$ † is defined as

$$\tilde{\chi}^2=\frac{\Sigma_i(E_i^{data}-E_i^{table})^2}{\Sigma_i E_i^{data}}. \tag{13}$$

The $\tilde{\chi}^2$ value has been calculated for each cluster and the $\tilde{\chi}^2$ cut has been applied after the reconstruction.

In the case that a cluster is wider than 3×3 counters, the reconstruction procedure for one γ-ray has been tried first. If the $\tilde{\chi}^2$ value is less than 0.01 GeV or the variance of this cluster is narrower than the variance calculated from the shower table, this cluster is regarded to be produced by one γ-ray. If these conditions are not satisfied, we consider that it contains two or more γ-rays. The reconstruction of two γ-rays is carried out in two stages of iteration. At the first stage, the parameters for the iteration are x and y positions of two γ-rays. The energy of each γ-ray is fixed to the half of the total energy deposit in a cluster. The step for each parameter is calculated using the difference between the variance of this cluster and the variance calculated from the shower table. The direction of each step is chosen to reduce this difference. When this difference becomes small, the second stage of the iteration starts. The parameters for this iteration are x and y positions and energies of two γ-rays. The step for each

† This $\tilde{\chi}^2$ is different from usual reduced χ^2. Assuming that the energy resolution of each counter can be parametrized as the energy resolution of CEMC detector (Eq. 4), $\tilde{\chi}^2$ is roughly equal to $0.03\times\chi^2$ at the total energy around 30 GeV. "χ^2 is equal to 1.0" corresponds roughly to "$\tilde{\chi}^2$ is equal to 0.03 GeV". In this $\tilde{\chi}^2$ definition, the influence from counters with small energy deposit is suppressed.

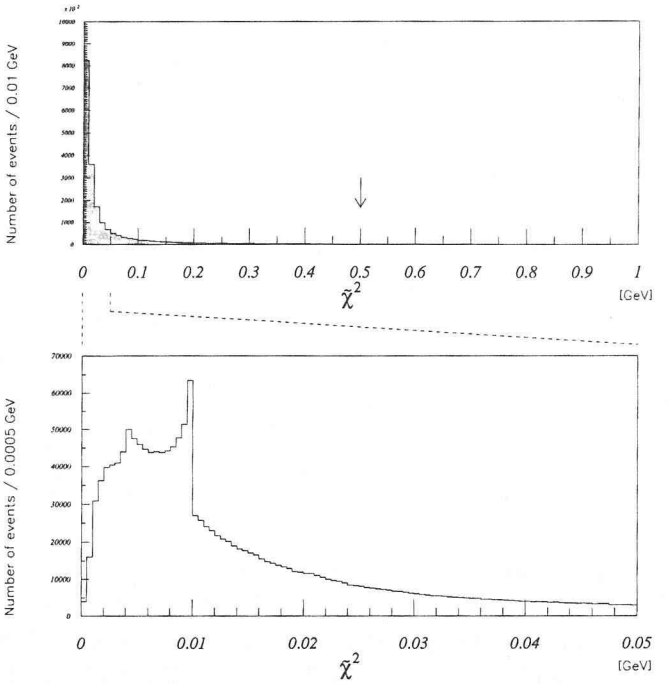

Fig. 13. The $\tilde{\chi}^2$ distribution after the reconstruction of shower data. The magnified figure is shown below for the small $\tilde{\chi}^2$ region.

parameter is calculated so as to decrease the $\tilde{\chi}^2$ value. This iteration finishes when the $\tilde{\chi}^2$ value reaches its minimum value or the $\tilde{\chi}^2$ becomes below 0.01 GeV. After this, expected energy deposit distribution from these two γ-rays has been subtracted from the cluster. The program has continued to search another γ-ray until the remaining energy of this cluster becomes the value lower than that of the cluster energy cut.

The $\tilde{\chi}^2$ distribution of this reconstruction method is shown in Fig. 13. The applied cut is $\tilde{\chi}^2<0.5$ GeV so as to keep as many real γ-rays as possible. 90% of γ-ray candidates has passed through this cut.

The fiducial cut and the energy cut have been also applied for selection of γ-ray candidates. Due to shower leakage, the reconstruction program is not able to provide correct results from the shower clusters which were near the edge of CEMC detectors. The fiducial cut has been applied for γ-rays whose x or y position is within 1.9 cm from the edge of CEMC. We have eliminated γ-rays with energy below 1.6 GeV to reduce fake γ-ray background. 70% of γ-ray candidates has passed through these cuts. The multiplicity distribution of γ-rays in both CEMC's is shown in Fig. 14.

4.3 Tracking of Charged Particles

The following procedure has been applied for obtaining the tracks of the charged particles from MWPC data. The position of fired wire for each MWPC plane is estimated by a straight line as

$$u_i=(a\cdot z_i+b)\cos\theta+(c\cdot z_i+d)\sin\theta, \tag{14}$$

where u_i indicates the distance between the fired wire and the z axis, z_i is the position of

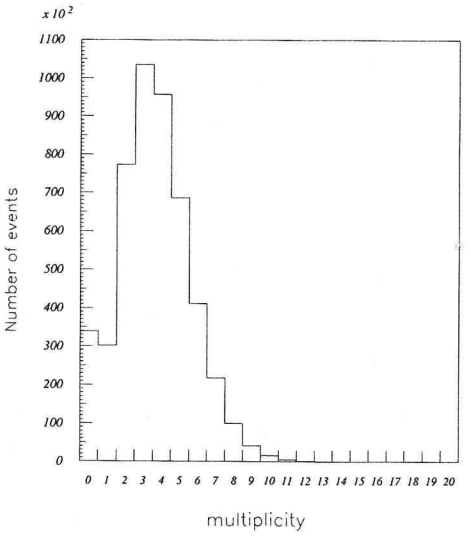

Fig. 14. Multiplicity distribution of reconstructed γ-rays.

the MWPC plane and θ indicates the angle of rotation of each plane of MWPC in the x-y plane. For x, y, u and v planes, θ angles are 0.0°, 90.0°, 28.1° and −28.1°, respectively. The fitting parameters, a, b, c and d have been derived so as to minimize χ^2 defined as

$$\chi^2=\sum_i\left(\frac{u_i^{data}-(a\cdot z_i+b)\cos\theta-(c\cdot z_i+d)\sin\theta}{(\text{wire spacing})}\right)^2. \tag{15}$$

The vertex position of the event has been reconstructed from tracks of scattered particles and the beam track. The distribution of vertex along z axis is shown in Fig. 15. The vertex finding efficiency is 33.6%. In the several data taking runs, the aluminum plate of 2 mm thick to protect PPT was placed, which is identified at 37 cm

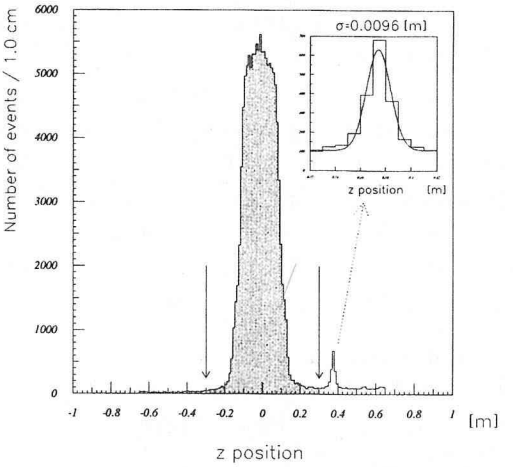

Fig. 15. The distribution of z positions of event vertices reconstructed from the data of MWPC's. The events with the z vertex within ±0.3 m from the target center have been selected. At 0.37 m downstream the target, the peak came from the aluminum plate of 2 mm thick.

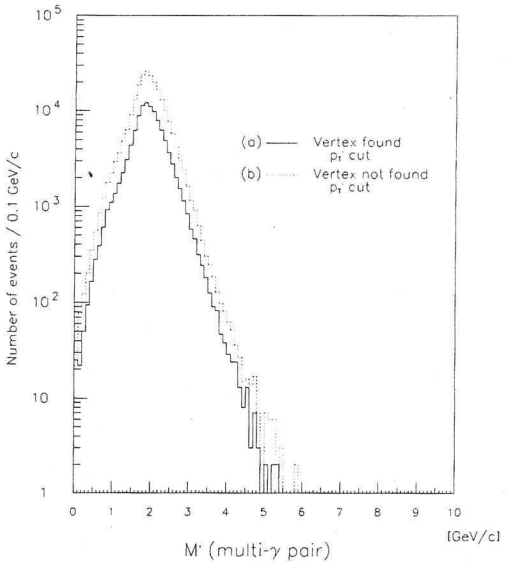

Fig. 16. The M' distribution of the events for the following cases. (a) Vertex found from MWPC data. (b) No vertex found from MWPC data.

from the target center as shown in Fig. 15. The width of this peak shows the vertex resolution of 0.96 cm (r.m.s.).

Once the vertex has been found, the events with the vertex position within ± 30 cm from the target center have been selected. 4.6% of events has been eliminated with this cut. The events in which vertices have not been found have been also picked up in order to obtain high statistics. In the case of multi-γ pairs, the M' distribution of events in which the vertices have not been found has almost the same slope as that of events in which the vertices have been found as shown in Fig. 16. The number of background events is, therefore, expected to be small in the events in which the vertices have not been found. The remaining background in the final data sample is thus 3% level.

4.4 Analysis of $\pi^0\pi^0$ Events

In this section, we explain the method to obtain $\pi^0\pi^0$ events including π^0 meson reconstruction and an applied cut for the energy asymmetry. We describe the evaluation of the correction factors for the derivation of the cross section for inclusive $\pi^0\pi^0$ production.

4.4.1 Selection of π^0 Mesons

To reconstruct $\pi^0 \rightarrow \gamma\gamma$, a decay position has been given by the vertex position found from MWPC data. When the vertex position has not been found, the center of the target has been used.

The invariant mass distribution of γ-ray pairs derived from 4-momentum vector of each γ-ray is shown in Fig. 17, together with the results of fits to determine the peaks of π^0 mass and the shapes of the background. After the background subtraction, the γ-ray pairs whose invariant mass is between 100 MeV/c^2 and 150 MeV/c^2 (for $p_T < 2.5$ GeV/c) or between 100 MeV/c^2 and 175 MeV/c^2 (for $p_T \geq 2.5$ GeV/c) have been

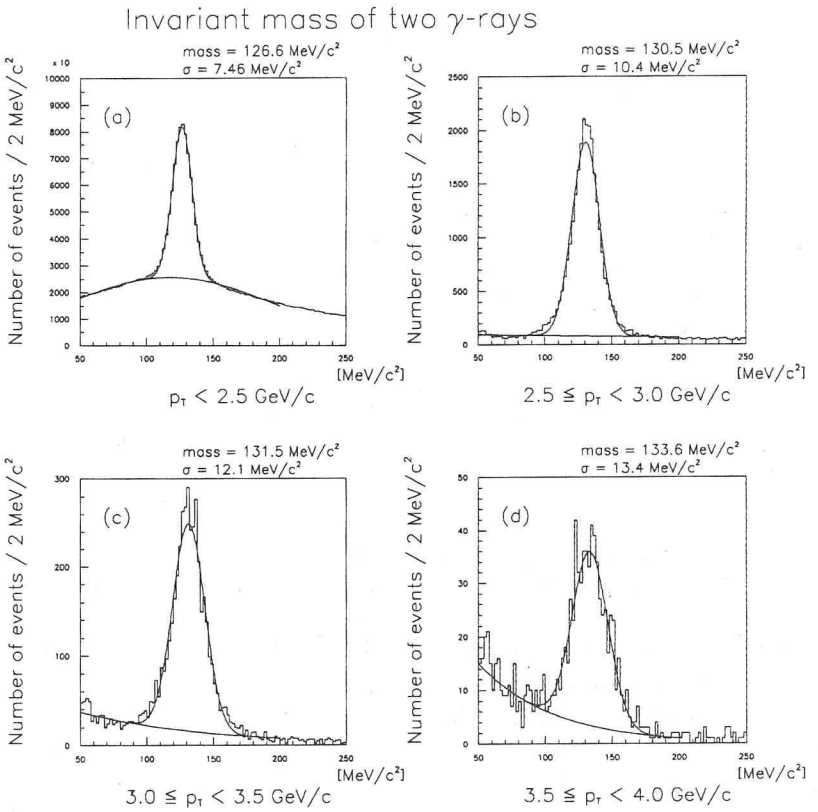

Fig. 17. The distribution of invariant mass of γ-ray pairs for different p_T's.

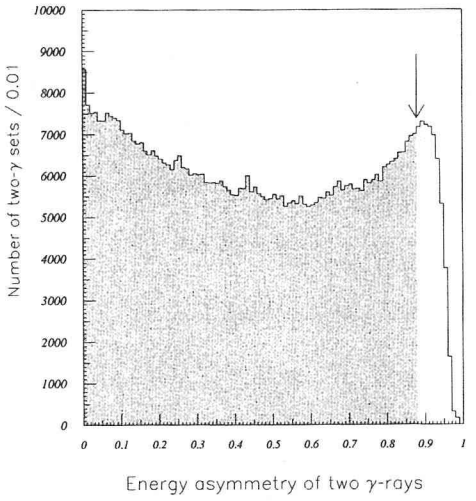

Fig. 18. The distribution of energy asymmetry of two γ-ray sets (π^0 mass region). The γ pairs with energy asymmetry below 0.88 have been selected.

regarded as π^0 mesons. For the shape of background, we have used an exponential function (for $p_T \geq 2.5$ GeV/c) or a Gaussian function (for $p_T < 2.5$ GeV/c).

The energy asymmetry of γ pairs in the π^0 mass region is shown in Fig. 18. We have applied a cut for the energy asymmetry as

$$|E^{\gamma_1} - E^{\gamma_2}|/(E^{\gamma_1} + E^{\gamma_2}) < 0.88. \tag{16}$$

Because some of low energy γ-rays have been eliminated by the cuts in the reconstruction of γ-rays, the reconstruction efficiency of π^0 mesons is low in the region in which the energy asymmetry is large. This cut has been applied to avoid such low-efficiency region. For the π^0 candidates, 91% of γ-ray pairs have remained after this cut.

4.4.2 Reconstruction Efficiency of π^0 Mesons

The reconstruction efficiency of π^0 mesons in the analysis program has been studied using the electromagnetic shower simulation package, EGS. The π^0 mesons with fixed p_T's ranging from 1.5 GeV/c to 4.2 GeV/c have been generated. Using the momenta and energies of two γ-rays from a π^0 meson as the input parameters for EGS, the data of electromagnetic showers have been produced. These data have been analyzed and the various cuts have been applied in the same way as the analysis of real data. The number of reconstructed π^0 mesons have been compared with that of generated π^0 mesons. In this Monte-Carlo study, the case that one of γ-rays from a π^0 meson missed the CEMC detector has been included, i.e. the reconstruction efficiency includes the geometrical detection efficiency. The results are shown in Fig. 19. In this figure, the error bars indicate statistical errors. The reconstruction efficiency, η_{π^0}, has been parametrized by a fit as

$$\begin{aligned}\eta_{\pi^0} = &-(0.332 \pm 0.007) \times \tanh\left[(1.29 \pm 0.02) p_T - (4.59 \pm 0.08)\right] \\ &+ (0.477 \pm 0.009)\end{aligned} \tag{17}$$

The error of each parameter in η_{π^0} comes from the fitting.

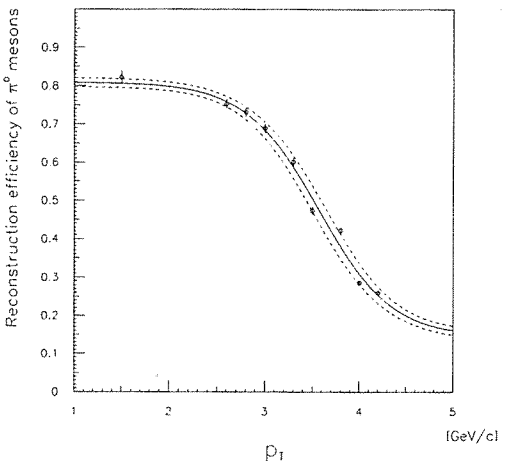

Fig. 19. The p_T dependence of reconstruction efficiency of π^0.

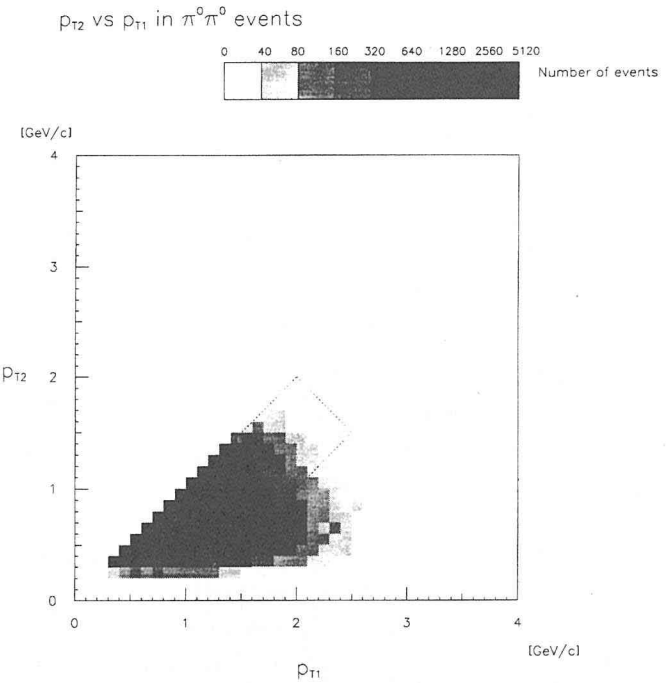

Fig. 20. Relation between p_{T_1} and p_{T_2} in $\pi^0\pi^0$ events. The higher p_T of π^0 is defined as p_{T_1} and the lower p_T of π^0 is defined as p_{T_2}. The $\pi^0\pi^0$ events within the rectangle have been picked up for the analysis.

In inclusive $\pi^0\pi^0$ production in the M' region between 2.5 GeV/c and 4.0 GeV/c and $|p_T'|<1.0$ GeV/c, p_T of each π^0 meson is less than 2.5 GeV/c as shown in Fig. 20. Consequently, the reconstruction efficiency of each π^0 meson is almost constant (≈ 0.8) in this M' region.

4.4.3 Correction for the p_T' Integration of $\pi^0\pi^0$

The p_T' distribution of the cross section for inclusive $\pi^0\pi^0$ production is known to be flat around $p_T'=0.0$ GeV/c and the distribution decreases steeply at large p_T' [21]. Our data have a similar tendency as shown in Fig. 21. The event distribution on p_T' in the region of M' between 2.5 GeV/c and 2.6 GeV/c is shown in this figure. At the first step in deriving the cross section for $p_T'=0$ GeV/c, the flat p_T' distribution has been assumed in the region of $|p_T'|<1.0$ GeV/c for the simplification. The difference between the real distribution on p_T' and the flat one has been corrected as follows. The event distribution has been fitted with the functions,

$$x=|p_T'|, \tag{18}$$

$$y=\begin{cases} A & (x<x_0) \\ -b(x-x_0)+A & (x\geq x_0) \end{cases}, \tag{19}$$

where A, b and x_0 are the fitting parameters and y is the number of events in each p_T' bin. The correction factor, $\xi_{\pi^0\pi^0}$, has been given as

$$\xi_{\pi^0\pi^0}=A/\bar{y}, \tag{20}$$

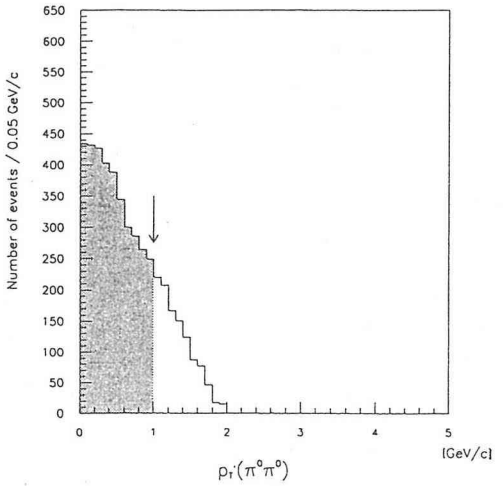

Fig. 21. The p_T' distribution of $\pi^0\pi^0$ events in the M' region between 2.5 GeV/c and 2.6 GeV/c.

Table 3. Correction factor of p_T' integration of $\pi^0\pi^0$ events

M' region [GeV]	$\xi_{\pi^0\pi^0}$
2.5–2.6	1.206±0.044
2.6–2.7	1.114±0.035
2.7–2.8	1.081±0.034
2.8–3.0	1.066±0.030
3.0–3.4	1.020±0.026
3.4–4.0	1.006±0.043

where $\bar{y}$ is the average value of y in $x<1.0$ GeV/c and is obtained from the data. The correction factors are obtained in each M' bin. The values are from 1.0 to 1.2 as shown in Table 3.

4.5 Analysis of Multi-γ Pair Events

We define "multi-γ" as a set of one or more γ-rays detected in one of the CEMC's, and the multi-γ pair event as an event in which multi-γ's are detected in both CEMC's. Monte-Carlo studies for inclusive multi-γ pair production have been carried out using PYTHIA (version 5.4) and JETSET (version 7.3) in the LUND simulation package in order to evaluate the correction factors for derivation of the cross section for inclusive multi-γ pair production. Reaction of partons in hard hadronic interactions are generated in PYTHIA. The fragmentation of outgoing partons is controlled in JETSET. The data of electromagnetic showers and hadronic showers are generated with GEANT (version 3.14) using the information of outgoing particles from JETSET. We have found that detected γ-rays are originated mainly in π^0 mesons (93%) and η mesons (6%).

4.5.1 M′ Correction

Multi-γ events include fake γ-rays from hadronic showers. In addition, electrons and positrons are not eliminated from the data because the MWPC data have not been used for the veto of charged particles due to their marginal efficiency. The relation between M' of multi-γ pair which has been reconstructed from shower data (M' *(reconstructed)*) and M' of multi-γ pair which put in the lead glass counters (M'*(input)*) has been obtained using the GEANT 3.14 and LUND simulation packages in order to evaluate such fake effects (Fig. 22) using the same procedure as in the real data. The relation between reconstructed p_T' and input p_T' has also been obtained in the same manner. The obtained correction functions are

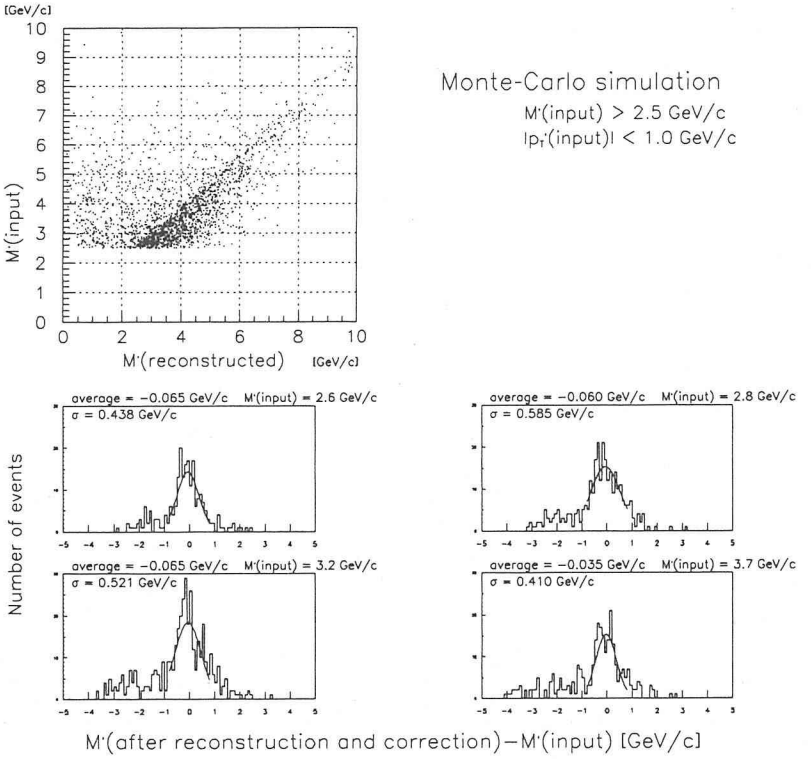

Fig. 22. Relation between reconstructed M' and input M' from the Monte-Carlo simulation.

$$M'(input) = 0.940M'(reconstructed) - 0.338 \text{ and} \tag{21}$$

$$p_T'(input) = 0.940 p_T'(reconstructed). \tag{22}$$

The uncertainty of M' due to this correction is estimated to be around 0.5 GeV/c.

4.5.2 *Reconstruction Efficiency of Multi-γ Pair*

We have studied the reconstruction efficiency of multi-γ pair events with a Monte-Carlo simulation. By comparing the distribution of the corrected M' of the reconstructed multi-γ pairs with the M' distribution of the input multi-γ pairs, the M' dependence of the reconstruction efficiency, η_{MGP}, has been obtained and is parametrized with a formula,

$$\eta_{MGP} = \frac{\exp\left[(6.21 \pm 0.11) - (0.652 \pm 0.023)M'\right]}{\exp\left[(6.26 \pm 0.19) - (0.620 \pm 0.045)M'\right]} \tag{23}$$

as shown in Fig. 23. The error of each parameter comes from the fitting of the input and reconstructed M' distributions. This correction is to cancel the response functions of the detector and the reconstruction procedure which produce a tail to lower M' from the input M' and lower the obtained cross section at the input M'.

4.5.3 *Acceptance Correction for Multi-γ*

Due to the finite size of the CEMC's, the geometrical detection efficiency for the multi-γ with given p_T becomes lower near the edge of the CEMC detector. To obtain the cross section for multi-γ pair at $x_F = 0$ with the ϕ angle difference of multi-γ's of 180°,

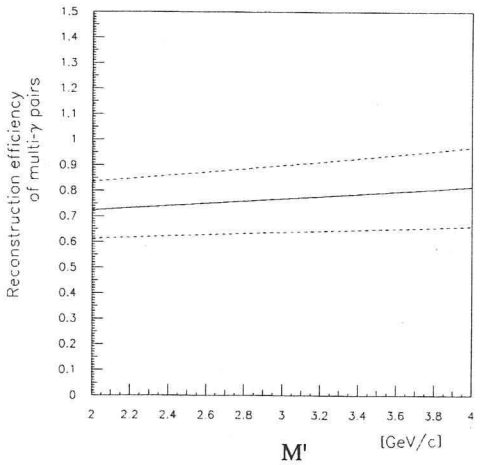

Fig. 23. The reconstruction efficiency of multi-γ pair. The dashed lines indicate the region of errors which comes from the fitting of input and reconstructed M' distribution.

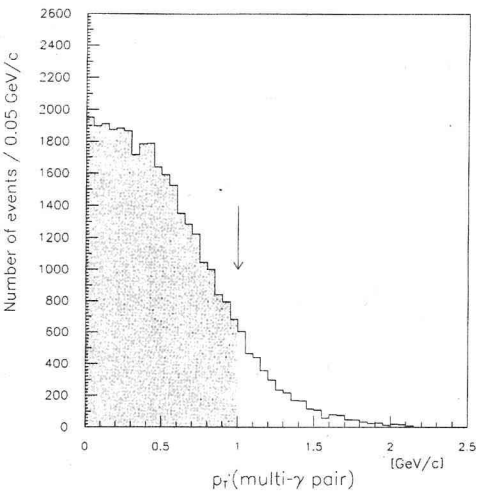

Fig. 24. The p_T' distribution of multi-γ pair events in the M' region between 2.0 GeV/c and 2.1 GeV/c.

the acceptance correction is required. At the first step in the derivation of the cross section, the flat distribution of multi-γ's on ϕ-x_F plane has been assumed for simplicity of integration. The difference between the real distribution and the flat one, therefore, has to be corrected by the detection efficiency (acceptance correction) which is obtained as a function of p_T using a simulation as described before. The obtained detection efficiency, ζ_{MG}, is given as

$$\zeta_{MG}=0.837\pm0.041, \tag{24}$$

which is almost constant in the region of p_T of multi-γ around 1 to 2 GeV/c.

4.5.4 *Correction for the p_T' Integration of Multi-γ Pair*

The same procedure as the $\pi^0\pi^0$ case has been applied to derive the cross section for $p_T'=0$ GeV/c. The p_T' distribution of the detected events is also flat around $p_T'=0.0$ GeV/c and it decreases steeply at large $|p_T'|$ value (Fig. 24). The p_T' distribution has been fitted with the functions,

$$x=|p_T'|, \tag{25}$$

$$y=p_1\{\tanh(p_2x+p_3)+1.0\}, \tag{26}$$

where p_1, p_2 and p_3 are the fitting parameters and y is the number of events in each p_T' bin. The correction factor, ξ_{MGP}, is given as

$$\xi_{MGP}=p_1\{\tanh(p_3)+1.0\}/\bar{y}, \tag{27}$$

where $\bar{y}$ is the average value of y in $x<1.0$ GeV/c and is obtained as the number of entries over the p_T' acceptance. The correction factors are obtained in each M' bin.

Table 4. Correction factor of p_T' integration of multi-γ pair events

M' region [GeV]	ξ_{MGP}
2.0–2.1	1.304±0.043
2.1–2.2	1.254±0.038
2.2–2.3	1.184±0.012
2.3–2.4	1.141±0.015
2.4–2.5	1.103±0.017
2.5–2.6	1.061±0.013
2.6–2.7	1.057±0.018
2.7–2.8	1.044±0.020
2.8–2.9	1.036±0.021
2.9–3.0	1.019±0.024
3.0–3.1	1.016±0.025
3.1–3.2	1.018±0.034
3.2–3.3	1.007±0.043
3.3–3.4	1.010±0.058
3.4–3.5	1.002±0.045
3.5–3.6	1.055±0.187
3.6–3.8	1.068±0.205

The values are 1.07 to 1.3 as shown in Table 4. The tendency of this correction factor is similar to the correction factor of $\pi^0\pi^0$.

5. Results and Discussion

We have derived the invariant double-differential cross sections for inclusive $\pi^0\pi^0$ production and inclusive multi-γ pair production. These cross sections have been compared with the results of a Monte-Carlo simulation. The A_{LL} for inclusive multi-γ pair production has been derived. Several theoretical models for $\Delta G/G$ have been compared with the present results.

5.1 Invariant Double-Differential Cross Section

The invariant double-differential cross sections are derived from the number of events as follows. The momenta of the pair, $\boldsymbol{p}_1$ and $\boldsymbol{p}_2$, are translated to transverse momenta, p_{T_1}, p_{T_2}, the Feynman's x's, x_{F_1}, x_{F_2} and azimuthal angles, ϕ_1, ϕ_2 as

$$E_1E_2\frac{d^6\sigma}{d\boldsymbol{p}_1{}^3d\boldsymbol{p}_2{}^3}=\frac{4}{s}\frac{d^6\sigma}{dp_{T_1}dp_{T_2}dx_{F_1}dx_{F_2}d\phi_1d\phi_2}. \tag{28}$$

Here, the following relations are used;

$$d\boldsymbol{p}^3=p^2\sin\theta d\theta dpd\phi, \tag{29}$$

$$pdpd\theta=dp_Tdp_L \text{ and} \tag{30}$$

$$dp_L=\frac{\sqrt{s}}{2}dx_F.$$

The observed cross section as a function of pseudo-mass, $\sigma(M')$, is described as

$$\sigma(M')=\int_{\Delta M'}\int_{\Delta p_T'}\int_{\Delta x_{F1}}\int_{\Delta x_{F2}}\int_{\Delta\phi_1}\int_{\Delta\phi_2}\frac{d^6\sigma}{dp_{T_1}dp_{T_2}dx_{F_1}dx_{F_2}d\phi_1d\phi_2}, \quad (32)$$

where $\Delta M'$ is a size of M' binning and $\Delta p_T'$ is an acceptance for the difference between p_{T_1} and p_{T_2} ($p_T'=|p_{T_1}|-|p_{T_2}|$). The Δx_{F_1}, Δx_{F_2}, $\Delta\phi_1$ and $\Delta\phi_2$ are the detector acceptances. The x_F acceptance is from $-0.035p_T$ to $0.0536p_T$, the ϕ acceptance is ±0.452 rad for CEMC1 and $\pi\pm0.452$ rad for CEMC2 and the p_T' acceptance is ±1.0 GeV/c. Therefore,

$$\begin{aligned}\sigma(M')&=\int_{\Delta M'}dM'\int_{-1.0}^{1.0}dp_T'\int_{-0.035p_{T2}}^{0.0536p_{T2}}dx_{F_2}\int_{-0.035p_{T1}}^{0.0536p_{T1}}dx_{F_1}\\&\cdot\int_{\pi-0.452}^{\pi+0.452}d\phi_2\int_{-0.452}^{0.452}d\phi_1\frac{d^6\sigma}{dp_{T_1}dp_{T_2}dx_{F_1}dx_{F_2}d\phi_1d\phi_2}\\&=\zeta^2\cdot\int_{\Delta M'}dM'\int_{-1.0}^{1.0}dp_T'(0.0886)^2p_{T_1}p_{T_2}(0.904)^2\\&\cdot\frac{d^6\sigma}{dp_{T_1}dp_{T_2}dx_{F_1}dx_{F_2}d\phi_1d\phi_2}\Big|_{x_{F1}=x_{F2}=0,\,\phi_1=0,\,\phi_2=\pi}\end{aligned} \quad (33)$$

where ζ^2 is the correction factor for the acceptance integration on the ϕ-x_F plane. Using the relations,

$$p_{T_1}p_{T_2}=(M'^2-p_T'^2)/4 \text{ and } dM'dp_T'=2dp_{T_1}dp_{T_2}, \quad (34)$$

we obtain

$$\begin{aligned}\sigma(M')&=\zeta^2\cdot\frac{(0.0886\times0.904)^2}{4}\int_{\Delta M'}dM'\int_{-1.0}^{1.0}dp_T'\cdot(M'^2-p_T'^2)\\&\cdot\frac{d^6\sigma}{dp_{T_1}dp_{T_2}dx_{F_1}dx_{F_2}d\phi_1d\phi_2}\Big|_{x_{F1}=x_{F2}=0,\,\phi_1=0,\,\phi_2=\pi}\\&=\frac{\zeta^2}{\xi(M')}\cdot\frac{(0.0886\times0.904)^2}{2}\\&\int_{\Delta M'}dM'\cdot M'^2\cdot\frac{d^6\sigma}{dp_{T_1}dp_{T_2}dx_{F_1}dx_{F_2}d\phi_1d\phi_2}\Big|_{x_{F1}=x_{F2}=0,\,\phi_1=0,\,\phi_2=\pi,\,p_T'=0}\end{aligned} \quad (35)$$

Here, $\xi(M')$ is the correction factor for p_T' integration. The number of detected events is related to the cross section as

$$\frac{N_{event}}{N_{beam}}\cdot\frac{A}{\rho lN_A}\cdot\frac{1}{D}=\varepsilon^2\sigma(M'), \quad (36)$$

where ε^2 is the reconstruction efficiency for the high-mass pair, N_{event} and N_{beam} are the total number of events and beam particles, respectively. The $A/(\rho lN_A)$ is the target constant and D is the dilution factor as described in Section 2.2.1. The cross section for inclusive hadron pair productions is known to be proportional to the atomic number[22]. Finally, we obtain

$$\begin{aligned}\frac{N_{event}}{N_{beam}}\cdot\frac{A}{\rho lN_A}\cdot\frac{1}{D}&=\frac{1}{\delta}\frac{(0.0886\times0.904)^2}{2}\cdot\int_{\Delta M'}dM'\cdot M'^2\\&\cdot\frac{d^6\sigma}{dp_{T_1}dp_{T_2}dx_{F_1}dx_{F_2}d\phi_1d\phi_2}\Big|_{x_{F1}=x_{F2}=0,\,p_T'=0,\,\phi_1=0,\,\phi_2=\pi}\end{aligned} \quad (37)$$

The parameter δ is given as

$$\delta=\frac{\xi(M')}{\varepsilon^2\zeta^2}=\begin{cases}\xi_{\pi^0\pi^0}/\eta_{\pi^0}^2 & (\text{for } \pi^0\pi^0)\\ \xi_{MGP}/(\eta_{MGP}\cdot\zeta_{MG}^2) & (\text{for multi-}\gamma\text{ pair})\end{cases}. \quad (38)$$

Here, η_{π^0} is the reconstruction efficiency of the π^0 meson evaluated in Section 4.4.2 including the acceptance correction, i.e. $\eta_{\pi^0}=\varepsilon\cdot\zeta$. The η_{MGP} is the reconstruction efficiency of multi-γ pair, i.e. $\eta_{MGP}=\varepsilon^2$, which is discussed in Section 4.5.2. The ζ_{MG} is the acceptance correction for multi-γ, which is described in Section 4.5.3. The $\xi_{\pi^0\pi^0}$ and ξ_{MGP} are the correction factors of p_T' integration for inclusive $\pi^0\pi^0$ production and inclusive multi-γ pair production, which are described in Section 4.4.3 and in Section 4.5.4. By introducing convenient definitions;

$$f(x_T,\sqrt{s})\equiv E_1E_2\frac{d^6\sigma}{d\boldsymbol{p}_1{}^3d\boldsymbol{p}_2{}^3}, \tag{39}$$

$$x_T=M'/\sqrt{s} \text{ and } \Delta x_T=\Delta M'/\sqrt{s}, \tag{40}$$

we obtain

$$\frac{N_{event}}{N_{beam}}\cdot\frac{A}{\rho l N_A}\cdot\frac{1}{D}$$
$$=\frac{(0.0886\times0.904)^2}{8}\cdot(\sqrt{s})^5\cdot\frac{1}{\delta}\int_{\Delta x_T}x_T{}^2f(x_T,\sqrt{s})dx_T. \tag{41}$$

Using an approximation of

$$\int_{\Delta x_T}x_T{}^2f(x_T,\sqrt{s})dx_T=\Delta x_T\cdot x_{T_0}{}^2f(x_{T_0},\sqrt{s})$$
$$(x_{T_0}=M'_0/\sqrt{s}), \tag{42}$$

the invariant double-differential cross section at x_{T_0} can be written as

$$f(x_{T_0},\sqrt{s})=\frac{N_{event}}{N_{beam}}\cdot\frac{A}{\rho l N_A}\cdot\frac{1}{D}$$
$$\cdot\frac{8}{(0.904\times0.0886)^2}\cdot\frac{1}{(\sqrt{s})^5}\cdot\delta\cdot\frac{1}{\Delta x_T\cdot x_{T_0}{}^2}. \tag{43}$$

The statistical error, $(\Delta f)_{stat}$, is evaluated as

$$(\Delta f)_{stat}=f\cdot\frac{\Delta N_{event}}{N_{event}}, \tag{44}$$

where the ΔN_{event} is the statistical error of the number of events. The systematic error, $(\Delta f)_{sys}$, is evaluated as

$$(\Delta f)_{sys}=f\cdot\sqrt{\left(\frac{\Delta\delta}{\delta}\right)^2+\left|\frac{\Delta(A/(\rho l N_A))}{(A/(\rho l N_A))}\right|^2+\left(\frac{\Delta N_{beam}}{N_{beam}}\right)^2+(w_{vertex})^2}, \tag{45}$$

where

$$\left(\frac{\Delta\delta}{\delta}\right)^2=(2\cdot\Delta\eta_{\pi^0}/\eta_{\pi^0})^2+(\Delta\xi_{\pi^0\pi^0}/\xi_{\pi^0\pi^0})^2 \tag{46}$$

for the $\pi^0\pi^0$ channel and

$$\left(\frac{\Delta\delta}{\delta}\right)^2=(\Delta\eta_{MGP}/\eta_{MGP})^2+(2\cdot\Delta\zeta_{MG}/\zeta_{MG})^2+(\Delta\xi_{MGP}/\xi_{MGP})^2 \tag{47}$$

for the multi-γ pair channel. The $\Delta(A/(\rho l N_A))$ is the systematic error of the target constant. The $\Delta\eta_{\pi^0}$ and $\Delta\eta_{MGP}$ are the systematic errors of the reconstruction efficiencies. The $\Delta\zeta_{MG}$ is the systematic error of the detection efficiency. The $\Delta\xi_{\pi^0\pi^0}$ and $\Delta\xi_{MGP}$ are the systematic errors of the correction factors for p_T' integration. The ΔN_{beam} is the systematic uncertainty of the total beam. The largest systematic uncertainty of the cross sections comes from the counting efficiency of beam protons and

is around 12%. Another source of the systematic error is the uncertainty of the target density, which is about 4%. As written in Section 4.3, the remaining background is about 3% of total events. The w_{vertex} indicates this uncertainty.

5.1.1. Inclusive $\pi^0\pi^0$ Production

The invariant double-differential cross section for inclusive $\pi^0\pi^0$ production has been obtained in the M' region between 2.5 GeV/c and 4.0 GeV/c and in the region of $|p_T'|<1.0$ GeV/c. The results are shown in Table 5 and Fig. 25. The total amount of the beam particles is 2.42×10^{10}. The overall normalization uncertainty, which is not included in this table, is about 13%. In addition to the systematic errors discussed in

Table 5. Invariant double-differential cross sections for inclusive $\pi^0\pi^0$ production. The first error indicates the statistical error and the second one is the systematic error

M' [GeV/c]	Cross section [pb/GeV$^4\cdot$c^6]
2.55	$(8.38\pm0.34\pm0.60)\times10^4$
2.65	$(5.81\pm0.26\pm0.85)\times10^4$
2.75	$(3.99\pm0.20\pm0.85)\times10^4$
2.90	$(2.54\pm0.11\pm0.29)\times10^4$
3.17	$(9.28\pm0.42\pm1.22)\times10^3$
3.63	$(1.87\pm0.14\pm0.14)\times10^3$

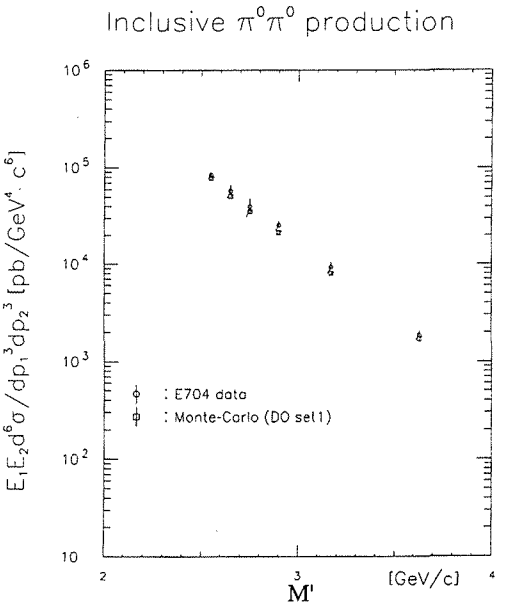

Fig. 25. The invariant double-differential cross section for inclusive $\pi^0\pi^0$ production compared with the Monte-Carlo results with the Duke-Owens Set 1.

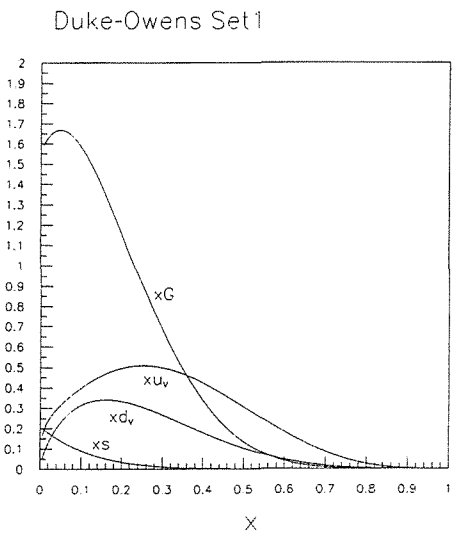

Fig. 26. The distribution functions of valence u-quark, valence d-quark, sea quark and gluon from the Duke-Owens Set 1.

the previous subsection, we include in Table 5 the ambiguity of the fitting procedure for the π^0 mass specta. In Fig. 25, the error bars indicate the quadratic sum of the statistical and the systematic errors in Table 5.

The Monte-Carlo simulation for inclusive $\pi^0\pi^0$ production has been carried out with PYTHIA and JETSET in the LUND Monte-Carlo simulation package. As the distribution functions of partons, the Duke-Owens (DO) Set 1[23] has been used. The functions of valence quarks and gluons in this model are written as

$$x(u_V+d_V)=1.874x^{0.419}(1-x)^{3.46}(1+4.4x), \tag{48}$$

$$xd_V=2.775x^{0.763}(1-x)^4, \tag{49}$$

$$xG=1.564(1+9x)(1-x)^6, \tag{50}$$

where x is the Bjorken's x (momentum fraction) and u_V, d_V and G indicate the distribution functions of valence u-quark, valence d-quark and gluon, respectively. The x distribution of them are shown in Fig. 26. In the present experimental condition ($\sqrt{s}=19.4$ GeV and $M'\approx 2.0\sim 4.0$ GeV/c), the Q^2 dependence of distribution functions can be ignored.

The following partonic processes have been taken into account to reproduce the data.

$$q+q'\to q+q',\ q+\bar{q}\to q'+\bar{q}',\ q+\bar{q}\to g+g$$
$$q+\bar{q}\to g+\gamma,\ q+\bar{q}\to \gamma+\gamma,\ q+g\to q+g$$
$$q+g\to q+\gamma,\ g+g\to q+\bar{q},\ g+g\to g+g$$

In the present experimental condition, the partonic processes,

$$q+q'\to q+q',\ q+g\to q+g,\ g+g\to g+g,$$

are found to contribute to about 90% of all detected events.

The results of the Monte-Carlo simulation are shown in Table 6 and Fig. 25. The values of the cross section from our experimental data and those from the Monte-Carlo results are found to be consistent.

The validity of the LUND fragmentation model with Duke-Owens Set 1 as the parton distribution functions in this energy region was also demonstrated in other

Table 6. Invariant double-differential cross sections for inclusive $\pi^0\pi^0$ production from the Monte-Carlo results using the Duke-Owens Set 1. The first error indicates the statistical error and the second one is the systematic error

M' [GeV/c]	Cross section [pb/GeV$^4\cdot$c^6]
2.55	$(7.80\pm0.22\pm0.28)\times10^4$
2.65	$(5.12\pm0.16\pm0.16)\times10^4$
2.75	$(3.55\pm0.13\pm0.11)\times10^4$
2.90	$(2.14\pm0.07\pm0.06)\times10^4$
3.17	$(8.02\pm0.26\pm0.20)\times10^3$
3.63	$(1.71\pm0.08\pm0.07)\times10^3$

Table 7. Invariant double-differential cross sections for inclusive multi-γ pair production. The first error indicates the statistical error and the second one indicates the systematic error

M' [GeV/c]	Cross section [pb/GeV$^4\cdot$c^6]
2.05	$(3.51\pm0.02\pm0.65)\times10^6$
2.15	$(2.54\pm0.02\pm0.47)\times10^6$
2.25	$(1.70\pm0.01\pm0.32)\times10^6$
2.35	$(1.17\pm0.01\pm0.22)\times10^6$
2.45	$(7.82\pm0.07\pm1.48)\times10^5$
2.55	$(5.22\pm0.06\pm0.99)\times10^5$
2.65	$(3.45\pm0.04\pm0.66)\times10^5$
2.75	$(2.33\pm0.03\pm0.45)\times10^5$
2.85	$(1.64\pm0.03\pm0.32)\times10^5$
2.95	$(1.05\pm0.02\pm0.21)\times10^5$
3.05	$(6.80\pm0.16\pm1.35)\times10^4$
3.15	$(5.00\pm0.14\pm1.01)\times10^4$
3.25	$(3.18\pm0.10\pm0.65)\times10^4$
3.35	$(2.18\pm0.08\pm0.46)\times10^4$
3.45	$(1.42\pm0.06\pm0.30)\times10^4$
3.55	$(1.09\pm0.06\pm0.30)\times10^4$
3.69	$(6.57\pm0.30\pm1.86)\times10^3$

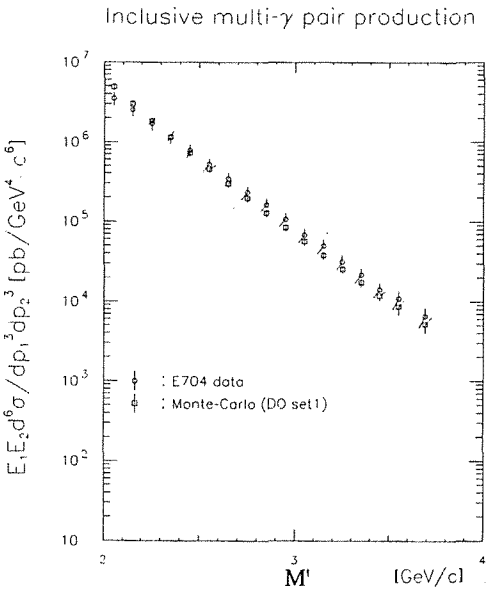

Fig. 27. The invariant double-differential cross section for inclusive multi-γ pair production is compared to the Monte-Carlo results with the Duke-Owens Set 1.

experiments. For example, NA22 at CERN which measured cross sections for inclusive π^0 production at $\sqrt{s}=21.7$ GeV[24] and NA24 at CERN which measured cross sections for the direct photon production and the π^0 production at $\sqrt{s}=23.7$ GeV[25] showed that the measured cross sections were consistent with their Monte-Carlo simulations.

NA24 measured cross sections for inclusive $\pi^0\pi^0$ production at $\sqrt{s}=23.7$ GeV[26]. The results of the present experiment have been compared with the results of NA24. The two experiments give almost consistent results.

5.1.2 Inclusive Multi-γ Pair Production

The invariant double-differential cross section for inclusive multi-γ pair production has been derived in the M' region between 2.0 GeV/c and 4.0 GeV/c and in the region of $|p_T'|<1.0$ GeV/c. The results are shown in Table 7 and Fig. 27. The total amount of the beam particles is 2.42×10^{10}. The systematic uncertainties, which mainly come from the ambiguity in the estimation of the reconstruction efficiency, is around 16%. The overall normalization uncertainty, which is not included in this table, is about 13%. In Fig. 27, the error bars indicate the quadratic sum of the statistical and the systematic errors in Table 7.

Using the same Monte-Carlo results as in the case of $\pi^0\pi^0$ events, the invariant double-differential cross section for inclusive multi-γ pair production has been obtained. The results are shown in Table 8 and Fig. 27. The values of the cross section from our

Table 8. Invariant double-differential cross sections for inclusive multi-γ pair production from the Monte-Carlo results using the Duke-Owens Set 1. The first error indicates the statistical error and the second one indicates the systematic error

M' [GeV/c]	Cross section [pb/GeV$^4\cdot$c^6]
2.05	$(4.89\pm0.04\pm0.51)\times10^6$
2.15	$(3.02\pm0.03\pm0.31)\times10^6$
2.25	$(1.84\pm0.02\pm0.18)\times10^6$
2.35	$(1.15\pm0.01\pm0.12)\times10^6$
2.45	$(7.26\pm0.11\pm0.73)\times10^5$
2.55	$(4.58\pm0.08\pm0.46)\times10^5$
2.65	$(3.00\pm0.07\pm0.30)\times10^5$
2.75	$(1.96\pm0.05\pm0.20)\times10^5$
2.85	$(1.29\pm0.04\pm0.13)\times10^5$
2.95	$(8.46\pm0.31\pm0.86)\times10^4$
3.05	$(5.65\pm0.24\pm0.58)\times10^4$
3.15	$(3.81\pm0.19\pm0.40)\times10^4$
3.25	$(2.56\pm0.15\pm0.28)\times10^4$
3.35	$(1.75\pm0.12\pm0.20)\times10^4$
3.45	$(1.19\pm0.10\pm0.13)\times10^4$
3.55	$(8.63\pm0.82\pm1.75)\times10^3$
3.69	$(5.17\pm0.44\pm1.12)\times10^3$

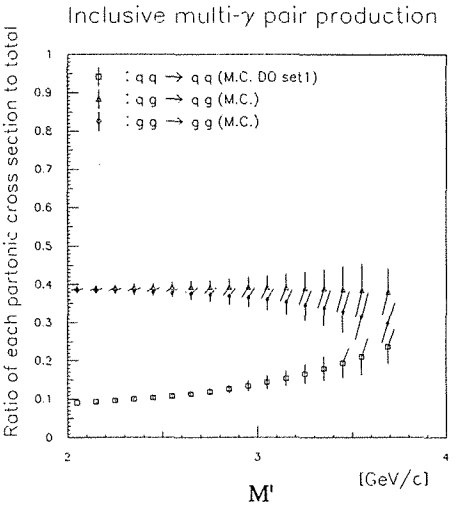

Fig. 28. The contributions of gluon-gluon, gluon-quark and quark-quark scatterings to the inclusive multi-γ pair production obtained from the Monte-Carlo simulation with the Duke-Owens set 1. The error bars indicate the statistical errors.

experimental data are consistent with those from the Monte-Carlo.

From this Monte-Carlo simulation with the Duke-Owens Set 1, contributions of gluon-gluon, gluon-quark and quark-quark scatterings to the multi-γ pair production have been obtained as shown in Fig. 28. The contributions are around 40% (gg), 40% (gq) and 9% (qq) in the region of M' between 2.0 GeV/c and 4.0 GeV/c. Therefore, gluon-gluon and gluon-quark scatterings can be considered as main partonic processes in our experimental condition.

The EHLQ Set 1[27] is another set of the typical parton distribution functions. This parametrization was originally proposed in order to investigate elementary particle reactions in the TeV energy region. The Monte-Carlo simulation with the EHLQ Set 1 was also performed for inclusive multi-γ pair production (Appendix A). The difference from the Duke-Owens Set 1 in the obtained cross sections is approximately 6%.

5.2 *Results of A_{LL} for Inclusive Multi-γ Pair Production*

The relation between A_{LL} and the numbers of events is given as

$$A_{LL}=\frac{1}{P_B}\frac{D}{P_T}\cdot\frac{N_{++}-N_{+-}}{N_{++}+N_{+-}} \tag{51}$$

The quantities, N's, are the normalized event rates measured in the same $(++)$ and

opposite $(+-)$ helicity combinations of beam and target protons in the center of mass frame. The P_B is the beam polarization and the P_T is the polarization of free protons in the target material. The D indicates the dilution factor as explained in Section 2.2.1. The A_{LL} values and their statistical errors have been derived run by run with the following formulae for each M' bin. For the positive target polarization,

$$A_{LL}=\frac{D}{P_B P_T}\frac{N_{++}-N_{-+}\kappa}{N_{++}+N_{-+}\kappa}, \tag{52}$$

$$\Delta A_{LL}=\frac{D}{P_B P_T}\frac{2\kappa}{(N_{++}+N_{-+}\kappa)^2}\sqrt{N_{++}N_{-+}\left\{N_{++}+N_{-+}+N_{++}N_{-+}\left(\frac{\Delta\kappa}{\kappa}\right)^2\right\}}. \tag{53}$$

For the negative target polarization,

$$A_{LL}=\frac{D}{P_B|P_T|}\frac{N_{--}\kappa-N_{+-}}{N_{--}\kappa+N_{+-}}, \tag{54}$$

$$\Delta A_{LL}=\frac{D}{P_B|P_T|}\frac{2\kappa}{(N_{--}\kappa+N_{+-})^2}\sqrt{N_{--}N_{+-}\left\{N_{--}+N_{+-}+N_{--}N_{+-}\left(\frac{\Delta\kappa}{\kappa}\right)^2\right\}}. \tag{55}$$

Here,

$$\kappa=\frac{N_{beam}{}^{+}}{N_{beam}{}^{-}} \text{ and } \left(\frac{\Delta\kappa}{\kappa}\right)^2=\frac{1}{N_{beam}{}^{-}}\left(1+\frac{1}{\kappa}\right), \tag{56}$$

and

D : dilution factor
P_B : beam polarization
P_T : target polarization
$N_{beam}{}^{+}$: amount of beam with positive P_B
$N_{beam}{}^{-}$: amount of beam with negative P_B
N_{++} : number of events with positive P_B and positive P_T
N_{+-} : number of events with positive P_B and negative P_T
N_{-+} : number of events with negative P_B and positive P_T
N_{--} : number of events with negative P_B and negative P_T

In order to study the systematic bias and to perform the run selection, false A_{LL} values have been derived for each run using the unpolarized region of the beam. In this case, the polarity of the snake magnets has been used in stead of the helicity of the beam proton. The false A_{LL} should be zero if there is no systematic drifts in the apparatus and no systematic geometrical bias. The discrepancy of the false A_{LL} from zero has been calculated using the formula as

$$\chi^2=\sum_i\left(\frac{A_{LL}{}^{false}}{\Delta A_{LL}{}^{false}}\right)^2, \tag{57}$$

where the summation is made over all four M' bins. The χ^2 distribution is shown in Fig. 29. We selected the runs with $\chi^2<40.0$.

After the run selection, the average values of A_{LL} have been derived with the p_T' cut ($|p_T'|<1.0$ GeV/c) as shown in Table 9 and Fig. 30. The error bars include the

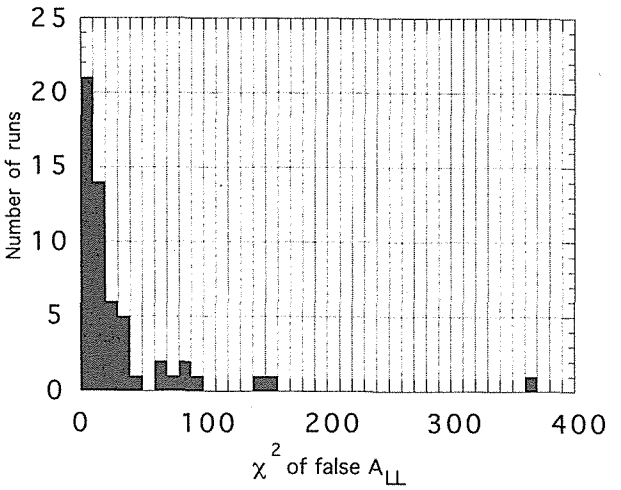

Fig. 29. The χ^2 distribution of the false A_{LL} for each run.

Table 9. The results of A_{LL} with $|p_T'|<1.0$ GeV/c

M' region [GeV/c]	Number of events	A_{LL}
2.0–2.2	12,488	-0.016 ± 0.186
2.2–2.4	8,118	-0.269 ± 0.230
2.4–3.0	8,710	-0.045 ± 0.222
3.0–4.0	1,477	-0.089 ± 0.531

Table 10. The results of false A_{LL} with $|p_T'|<1.0$ GeV/c

M' region [GeV/c]	Number of events	False A_{LL}
2.0–2.2	17,202	-0.019 ± 0.158
2.2–2.4	10,967	-0.008 ± 0.198
2.4–3.0	11,806	-0.139 ± 0.190
3.0–4.0	2,000	-0.421 ± 0.459

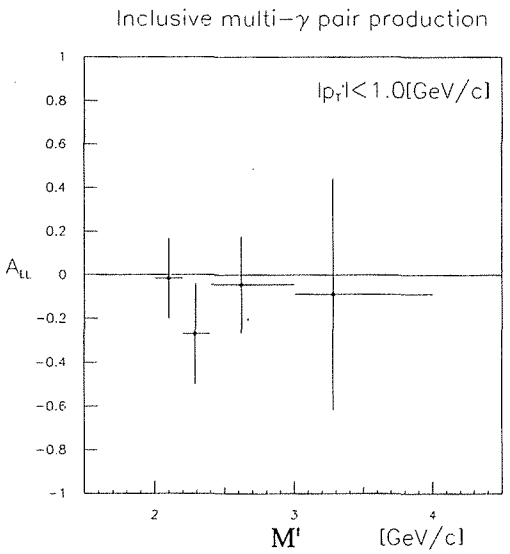

Fig. 30. A_{LL} for inclusive multi-γ pair production as a function of pseudo-mass, M', with $|p_T'|<1.0$ GeV/c.

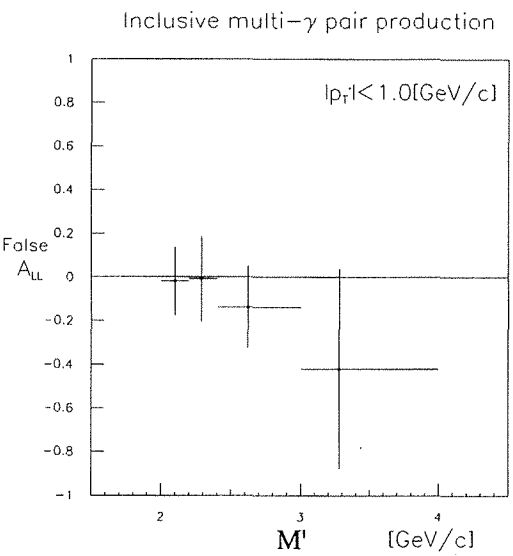

Fig. 31. False A_{LL} for inclusive multi-γ pair production.

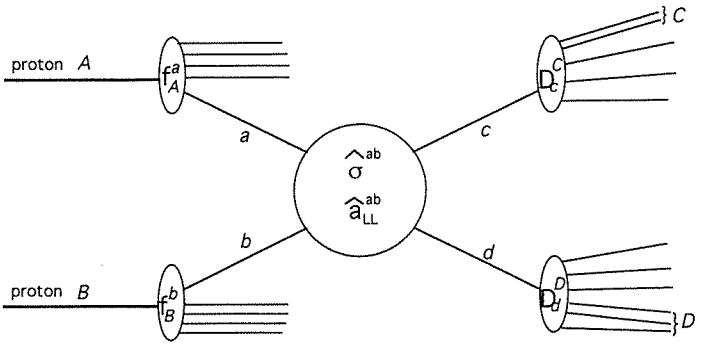

Fig. 32. The parton picture of hard collision of protons. The partons a and b collide and create the partons c and d following by fragmentation processes, D_c^C and D_d^D, to produce the final states C and D.

statistical ones only. The measured A_{LL} values are consistent with zero.

The false A_{LL} of all selected runs is also evaluated. The results are shown in Table 10 and Fig. 31. The error bars indicate statistical ones only. These values are also consistent with zero.

5.3 Theoretical Calculations of A_{LL}

Based on the parton collision model as shown in Fig. 32, the formula of A_{LL} is written as

$$A_{LL}=\frac{\Sigma_{a,b,c,d}\int_{\text{phase space}}^{\text{parton}}\Delta f_A^a(x_a,Q^2)\Delta f_B^b(x_b,Q^2)D_c^C(z_c,Q^2)D_d^D(z_d,Q^2)\hat{a}_{LL}^{ab}d\hat{\sigma}^{ab}/d\hat{t}}{\Sigma_{a,b,c,d}\int_{\text{phase space}}^{\text{parton}}f_A^a(x_a,Q^2)f_B^b(x_b,Q^2)D_c^C(z_c,Q^2)D_d^D(z_d,Q^2)d\hat{\sigma}^{ab}/d\hat{t}}. \quad (58)$$

The f_A^a indicates the distribution function of the parton a in the proton A and the Δf_A^a is its spin dependent distribution function. The $\hat{a}_{LL}^{ab}$ is the double-helicity asymmetry for the partonic process between a and b[28]. The amplitude of $\hat{a}_{LL}$ as a function of the scattering angle, θ, is shown in Fig. 33. The D_c^C indicates the fragmentation function of the parton c into the final state C. The summation is carried out for all the configurations of a, b, c and d. The integration is carried out in the phase space of partons.

The Duke-Owens Set 1[23] has been used as the distribution functions of partons and the Carlitz-Kaur model[28,29] has been used as the spin dependent distribution functions of quarks. Concerning the gluon polarization, six types of the models [15,16,17,18,19] have been considered.

The parton distribution functions in the Duke-Owens Set 1 were described in Eqs. 48, 49 and 50. According to the Carlitz-Kaur model, the spin dependent distribution functions of valence quarks in a proton are written as

$$\Delta u_V=\left[u_V-\frac{2}{3}d_V\right]\cos 2\theta \text{ and} \quad (59)$$

$$\Delta d_V=-\frac{1}{3}d_V\cos 2\theta \text{ with} \quad (60)$$

$$\cos 2\theta=\frac{1}{1+0.052(1-x)^2/\sqrt{x}}, \quad (61)$$

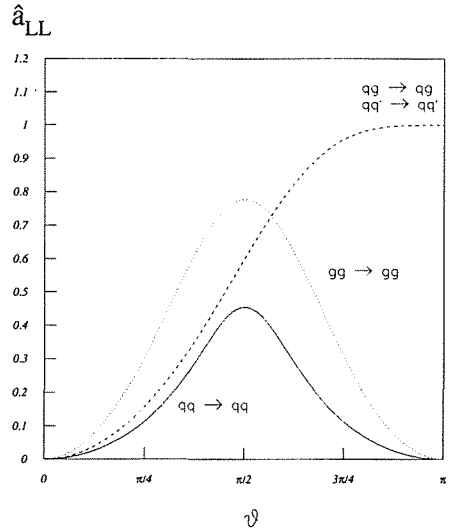

Fig. 33. The double-helicity asymmetry, $\hat{a}_{LL}$, of the partonic processes, $g+g\to g+g$, $q+g\to q+g$, $q+q\to q+q$ and $q+q'\to q+q'$.

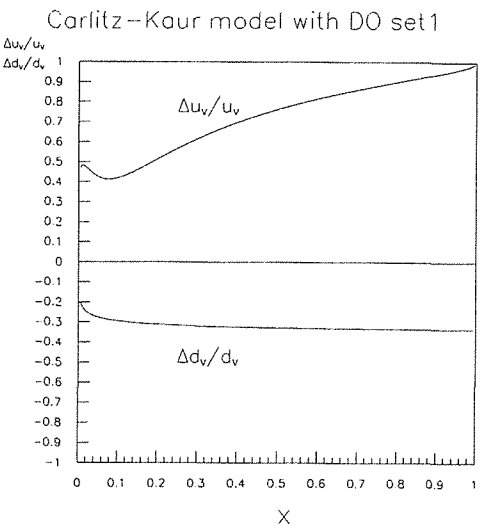

Fig. 34. The polarization distribution of valence u-quark and d-quark obtained from the Carlitz-Kaur model with the Duke-Owens Set 1.

where Δu_V and Δd_V indicate the spin dependent distribution functions of u-quark and d-quark in valence components, respectively. The graphs of $\Delta u_V/u_V$ and $\Delta d_V/d_V$ are shown as functions of x in Fig. 34. In this model, sea quarks are assumed to be unpolarized.

The model formulae of the gluon polarization, $\Delta G/G$, are listed in Table 11, and the numerical values of them are shown as functions of x in Fig. 35. In all the models other than (v) and (vi), ΔG's are parametrized by adopting Duke-Owens Set 1 as the spin averaged parton distribution. In the model (vi), KMRS B$_-$[30] is adopted for the same purpose. In the model (v), EHLQ Set 1[27] is adopted. Among many sets of parton distribution functions, Duke-Owens Set 1 has been chosen in order to set up the common conditions except for the shape of $\Delta G/G$.

For the numerical evaluation of A_{LL}, we have used the data of multi-γ pair events generated in the LUND Monte-Carlo simulation to perform the summation for all

Table 11. $\Delta G/G$ models

	$\Delta G/G$	Author(s)	Reference
(i)	x	G. Ramsey and D. Sivers	[15]
(ii)	$12.5x(x\leq 0.08)$ $1.0(x>0.08)$	G. Ramsey and D. Sivers	[15]
(iii)	$5x(x\leq 0.2)$ $1.0(x>0.2)$	E.L. Berger and J. Qiu	[16]
(iv)	$\dfrac{16.3x^{0.7}(1-x)}{1.564(1+9x)}$	G. Altarelli and W.J. Stirling	[17]
(v)	$22x(1-x)^{10}$	Z. Kunszt	[18]
(vi)	$6.208x^{0.6}(1-x)^{14}$	T. Morii, S. Tanaka and T. Yamanishi	[19]

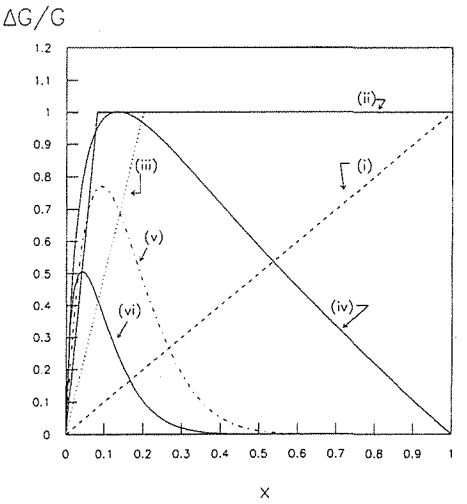

Fig. 35. The models of $\Delta G/G$ used in the A_{LL} calculations, (i) from Ref. 15, (ii) from Ref. 15, (iii) from Ref. 16, (iv) from Ref. 17, (v) from Ref. 18 and (vi) from Ref. 19.

parton configurations and the integration of the parton phase space. For each Monte-Carlo event, expected A_{LL} value has been calculated using $\hat{a}_{LL}$ and the parton distribution functions (Duke-Owens set 1, the Carlitz-Kaur model and each $\Delta G/G$ model). The average has been obtained. The results are shown in Fig. 36.

The histogram in Fig. 37 shows the x distribution of gluons which contribute to the

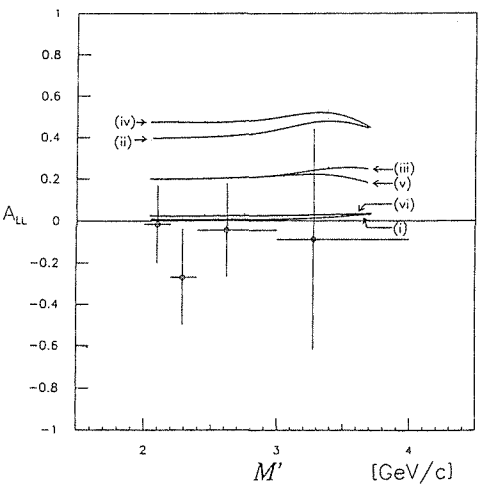

Fig. 36. The theoretical calculations of A_{LL} compared with the present results. The $\Delta G/G$ functions, (i), (ii), (iii), (iv), (v) and (vi), are used for the calculations.

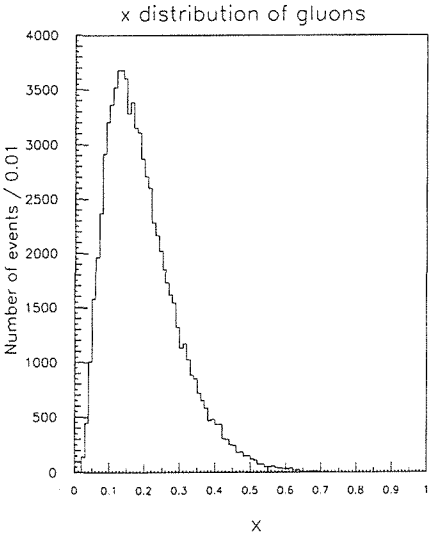

Fig. 37. The x distribution of gluons which contribute to the multi-γ pair production, obtained by the Monte-Carlo simulation with the Duke-Owens Set 1.

multi-γ pair production, obtained by the Monte-Carlo simulation. Since the contribution of gluons is larger than that of quarks in $2.0<M'<4.0$ GeV/c as mentioned in Section 5.1.2, the gluons in the region of $0.05\lesssim x\lesssim 0.35$ play an important role in our measurement of inclusive multi-γ pair production and its asymmetry. As shown in Fig. 36, the $\Delta G/G$ models (i) and (vi) are consistent with our results. On the other hand, models like (ii) and (iv) are not consistent.

The theoretical calculations of A_{LL} with EHLQ Set 1 have been also carried out (Appendix A). The results of the theoretical estimations of A_{LL} using EHLQ Set 1 have similar tendency with those using Duke-Owens Set1.

5.4 Conclusion

The measurements of the cross sections for inclusive $\pi^0\pi^0$ production and inclusive multi-γ pair production have been presented. The invariant double-differential cross sections for those interactions are consistent with the results of the LUND Monte-Carlo simulation.

The A_{LL} for inclusive multi-γ pair production has been derived. The values are consistent with zero. The A_{LL} values presented here are sensitive to $\Delta G/G$ in proton. By comparing our results with the theoretical calculations, we set a limit to the shape and the magnitude of $\Delta G/G$ in the region of $0.05\lesssim x\lesssim 0.35$. The experimental results are not consistent with the models which assume large $\Delta G/G$ around this x region.

Acknowledgements

First of all, the author would like to thank Prof. A. Masaike for the careful advice, the continuous encouragement and helpful discussions to accomplish this work.

He also would like to thank Profs. H. En'yo, K. Imai and A. Yokosawa for their helpful advice throughout the experiment and the analyses.

He wants to say his great thanks to Profs. R. Takashima, F. Takeutchi, T. Yoshida, S.B. Nurushev, A.N. Vasiliev and Dr. N. Saito for their useful suggestions.

He is grateful to many theorists. In particular, he would like to say his thanks to Prof. K. Hidaka at Tokyo Gakugei University and Prof. T. Morii and Dr. T. Yamanishi at Kobe University. Also, he would like to say his thanks to Dr. D. Sivers for the theoretical discussion.

The experiment described in this thesis has been carried out by the combined effort of many individuals in the FNAL-E704 collaboration. The following are the collaborators.

D.L. Adams, N. Akchurin, N.I. Belikov, A. Bravar, J. Bystricky, P. Chaumette, M.D. Corcoran, J.D. Cossairt, J. Cranshaw, J. Deregel, A.A. Derevschikov, G. Durand, H. En'yo, J. Fabre, K. Fukuda, H. Funahashi, Y. Goto, O.A. Grachov, D.P. Grosnick, D.A. Hill, T. Iijima, K. Imai, Y. Itow, K. Iwatani, T. Kasprzyk, K.W. Krueger, K. Kuroda, M. Laghai, F. Lehar, A. de Lesquen, D. Lopiano, F.C. Luehring, T. Maki, A. Masaike, Yu.A. Matulenko, A.P. Meschanin, A. Michalowicz, D.H. Miller, K. Miyake, T. Nagamine, F. Nessi-Tedaldi, M. Nessi, C. Nguyen, S.B. Nurushev, Y. Ohashi, Y. Onel, D.I. Patalakha, G. Pauletta, A. Penzo, A.L. Read, J.B. Roberts, L. van Rossum,

V.L. Rykov, N. Saito, G. Salvato, P. Schiavon, J. Shepard, J. Skeens, V.L. Solovyanov, H. Spinka, R. Takashima, F. Takeutchi, N. Tamura, N. Tanaka, D.G. Underwood, A.N. Vasiliev, A. Villari, J.L. White, S. Yamashita, A. Yokosawa, T. Yoshida and A. Zanetti

He really appreciates all the efforts made by the collaborators.

One of E704 members, Dr. N. Tanaka, has passed away in February, 1991. Also, one of our colleague, Dr. A. Villari, has passed away recently. He prays for the repose of their souls.

The author would like to say his thanks to the staff of Fermi National Accelerator Laboratory (FNAL) for supporting the present experiment.

He expresses his thanks to Dr. M. Mishina of KEK for the continuous support to carry out this experiment.

He would like to thank to the Ministry of Education, Science and Culture in Japan, the USSR Ministry of Atomic Power and Industry, the US Department of Energy, the Commissariat a l'Energie Atomique and the Institut National de Physique Nucleaire et de Physique des Particules in France, and the Istituto di Fisica Nucleare in Italy for supporting the present research. He would like to thank specially to the JSPS Fellowships for Japanese Junior Scientists for supporting his research.

Finally, he would like to thank to his parents for their support throughout his studies.

References

[1] R.D. Klem et al., *Phys. Rev. Lett.*, **36**, 929 (1976).
W.H. Dragoset, Jr. et al., *Phys. Rev. D*, **18**, 3939 (1978).
[2] For example,
B.E. Bonner et al., *Phys. Rev. D*, **38**, 729 (1988).
B.E. Bonner et al. *Phys. Rev. Lett.* **62** 1591 (1989).
[3] J. Antille et al., *Phys. Lett. B*, **94**, 523 (1980).
[4] V.D. Apokin et al., *Phys. Lett. B*, **243**, 461 (1990).
[5] M.J. Alguard et al., *Phys. Rev. Lett.*, **41**, 70 (1978).
G. Baum et al., *Phys. Rev. Lett.*, **51**, 1135 (1983).
[6] J. Ashman et al., *Phys. Lett. B*, **206**, 364 (1988).
[7] B. Adeva et al., *Phys. Lett. B*, **302**, 533 (1993).
D. Adams et al., *Phys. Lett. B*, **329**, 399 (1994).
[8] P.L. Anthony et al., *Phys. Rev. Lett.*, **71**, 959 (1993).
[9] J.D. Bjorken, *Phys. Rev.*, **148**, 1467 (1966).
J.D. Bjorken, *Phys. Rev. D*, **1**, 1376 (1970).
S.A. Larin and J.A.M. Vermaseren, *Phys. Lett. B*, **259**, 345 (1991).
[10] J. Ellis and R. Jaffe, *Phys. Rev. D*, **9**, 1444 (1974).
J. Ellis and R. Jaffe, *Phys. Rev. D*, **10**, 1669 (1974).
J. Kodaira et al., *Phys. Rev. D*, **20**, 627 (1979).
J. Kodaira et al., *Nucl. Phys.B*, **159**, 99 (1979).
J. Kodaira, *Nucl. Phys. B*, **165**, 129 (1980).
[11] M. Karliner, Proceedings of the Symposium on Future Polarization Physics at Fermilab (edited by E. Berger, J.G. Morfin, A.L. Read and A. Yokosawa) p. 1.
[12] D.L. Adams et al., *Phys. Lett. B*, **261**, 197 (1991).
[13] D. Indumathi et al., *Z. Phys. C*, **56**, 427 (1992).
[14] D. L. Adams et al., *Phys. Lett. B*, **336**, 269 (1994).

[15] G. Ramsey and D. Sivers, *Phys. Rev. D*, **43**, 2861 (1991).
[16] E.L. Berger and J. Qiu, *Phys. Rev. D*, **40**, 778 (1989).
[17] G. Altarelli and W.J. Stirling, Particle World Vol. 1 40 (1989).
[18] Z. Kunszt, *Phys. Lett. B*, **218**, 243 (1989).
[19] T. Morii, S. Tanaka and T. Yamanishi, *Phys. Lett. B*, **322**, 253 (1994), KOBE-FHD-94-02
[20] D.P. Grosnick et al., *Nucl. Inst. and Meth. A*, **290**, 269 (1990).
During the beam time in 1987, the center value of beam momentum was 185 GeV/c because of the magnet setting.
[21] H. Jöstlein et al., *Phys. Rev. D*, **20**, 53 (1979).
[22] R.L. McCarthy et al., *Phys. Rev. Lett.*, **40**, 213 (1978).
V.V. Abramov et al., *Sov. J. Nucl. Phys.*, **34**, 706 (1981).
V.V. Abramov et al., *JETP Lett.*, **38**, 352 (1983).
K. Streets et al., *Phys. Rev. Lett.*, **66**, 864 (1991).
P.B. Straub et al., *Phys. Rev. Lett.*, **68**, 452 (1992).
[23] D.W. Duke and J. F. Owens, *Phys. Rev. D*, **30**, 49 (1984).
[24] I.V. Ajinenko et al., *Z. Phys. C*, **35**, 7 (1987).
[25] C. De Marzo et al., *Phys. Rev. D*, **36**, 8 (1987).
C. De Marzo et al., *Phys. Rev. D*, **36**, 16 (1987).
[26] C. De Marzo et al., *Phys. Rev. D*, **42**, 748 (1990).
[27] E. Eichten, I. Hinchliffe, K. Lane and C. Quigg, *Rev. of Mod. Phys.* 56 579 1984, *Rev. of Mod. Phys.*, **58**, 1065 (1985).
[28] N.S. Craigie, K. Hidaka, M. Jacob and F.M. Renard, *Phys. Rep.*, **99**,, 69 (1983).
[29] R. Carlitz and J. Kaur, *Phys. Rev. Lett.*, **38**, 673 (1977).
[30] J. Kwiecinski, A.D. Martin, W.J. Stirling and R.G. Roberts, *Phys. Rev. D*, **42**, 3645 (1990).

Appendix

A Monte-Carlo simulation using EHLQ Set1

The EHLQ Set 1 is one of the typical sets of parton distribution functions. In this appendix, the results of the Monte-Carlo simulation with the EHLQ Set 1 are shown.

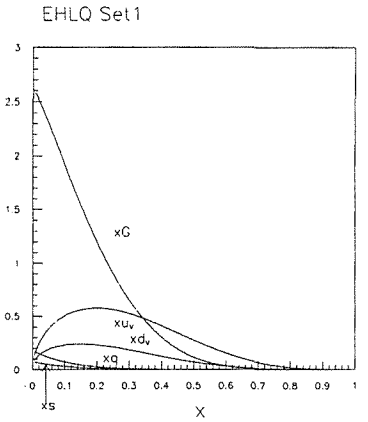

Fig. 38. The distribution functions of valence *u*-quark, valence *d*-quark, strange quark, sea quark and gluon from the EHLQ set 1.

The distribution functions of valence quarks and gluons in a proton in the EHLQ Set 1 are shown in Fig. 38. The model functions are given as

$$xu_V = 1.78x^{0.5}(1-x^{1.51})^{3.5}, \tag{62}$$

$$xd_V = 0.67x^{0.4}(1-x^{1.51})^{4.5}, \tag{63}$$

$$xG = (2.62+9.17x)(1-x)^{5.90}. \tag{64}$$

The Monte-Carlo similation with the EHLQ Set 1 has bean done in the same way as that with the Duke-Owens Set 1. The results are shown in Fig. 39. The Monte-Carlo results well reproduce the data.

The theoretical calculations of A_{LL} with the EHLQ Set 1 have been studied in the same way in the main text.

As shown in Fig. 40, these results have similar tendency as the Duke-Owens Set 1.

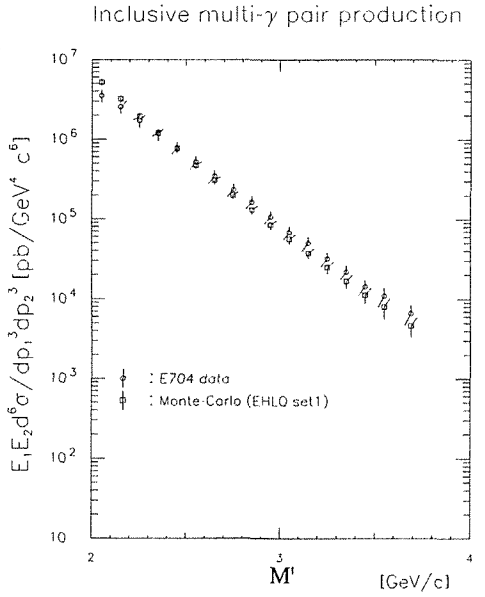

Fig. 39. The invariant double-differential cross section for inclusive multi-γ pair production is compared to the Monte-Carlo results with the EHLQ Set1.

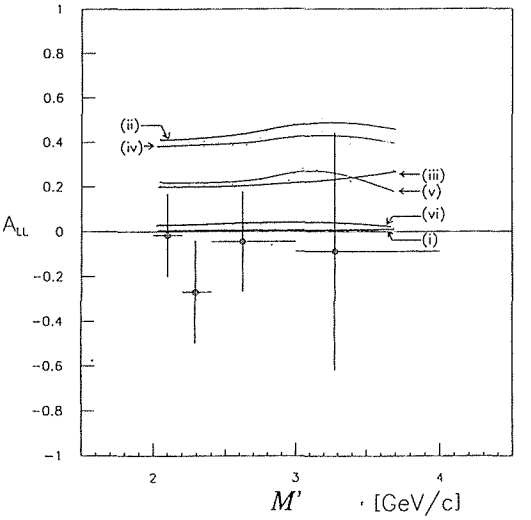

Fig. 40. The theoretical calculations of A_{LL} with the EHLQ Set1 compared with the present results. The $\Delta G/G$ functions, (i), (ii), (iii), (iv), (v) and (vi), are used for the calculations.